The University of Nottingham

NMR Relaxation in Solid ^{129}Xe

By

Rupa Jagannathan, B.E.

Dissertation submitted to the University of Nottingham

For the degree of Master of Research, September 2003

ABSTRACT

Spin-polarised ^{129}Xe can be used as a contrast agent to increase the sensitivity of Magnetic Resonance Imaging. For this purpose, ^{129}Xe has been polarised by the brute-force method and nuclear magnetic resonance (NMR) experiments have been performed on solid ^{129}Xe. Polarisations of 40% can be achieved at high magnetic fields of about 15T and ultra low temperatures below 100mK. Unfortunately, the spin-lattice relaxation time T_1 increases with an increase in the magnetic field and temperature ratio *(B/T)* and at the high fields and low temperatures, at which it was hoped to achieve polarisation, T_1 becomes inordinately high. Thus, a relaxation switch, consisting of paramagnetic oxygen, has been developed to accelerate the relaxation process by strong coupling of its large electronics dipole moment to the xenon nuclei.

The details of the equipment necessary for this project are presented. In particular the ^{3}He-^{4}He dilution refrigerator, which cools down the sample to ultra-low temperatures and the super conducting magnets, which provide the static magnetic field are described as are the spectrometer and coupling circuits.

As temperature control and measurement is a vital aspect of this project, the subject of field independent, low temperature thermometry has been treated in detail. Specifically, apart from the RuO_2 resistance thermometer and Coulomb Blockade thermometer, the possibility of using a quartz tuning fork in thermometry has been studied and the experimental results of its behaviour under different conditions of temperature, pressure and the medium in which it is immersed, are reported.

ACKNOWLEDGEMENTS

This project was very much a team-effort and I would like to take this opportunity to thank the members of our team and the various other people who have helped me during my course.

Firstly, I would like to thank my supervisor Dr. John Owers-Bradley for giving me the opportunity to work on this project. His guidance and timely appraisals of my work helped me complete it on time. I am especially grateful for his patience and understanding in all matters.

I am particularly indebted to Dr. Eugenii Krjukov for all his advice in countless discussions. Without his help and mentoring, the completion of this project would have been impossible.

My profound gratitude to Mr. Malcolm Carter and Mr. Christopher Pallender for their assistance with the dilution refrigerator and Mr. Robert Chettle for constructing the spectrometer.

Many thanks to Rob Nyman, who is one of the most helpful persons I have ever met, always ready to lend a hand, good advice or just to have a great time with. Thanks for proof-reading in detail. The same holds true for Rajeev Kini, who has proof-read almost every chapter and has spent countless hours listening when I needed someone to hear me out.

I would like to thank my family for their never-ending support, love and encouragement in everything I do.

Finally a big Thank You to Abhi…I couldn't have done it without you.

CONTENTS

Abstract **i**

Acknowledgements **ii**

Contents **iii**

1 Introduction 1

1.1 Comparison of ^{129}Xe and ^{3}He 2

1.2 Method of Polarisation 2

1.3 The Relaxation Switch 3

1.4 Scope of Project 4

2 Principles of Nuclear Magnetic Resonance 6 2.1

Method of Magnetic Resonance 6

2.2 Relaxation Times 11

2.2.1 Spin-Lattice Relaxation 11

2.2.2 Spin-Spin Relaxation 12

2.3 Pulse Sequences 13

2.3.1 Saturation Recovery 13

2.3.2 Inversion Recovery 13

2.3.4 Spin Echo 14

2.4 Chemical Shift 15

3 The ^{3}He-^{4}He Dilution Refrigerator 16

3.1 Principle of Operation 16

3.2 Cooling Procedure 19

3.3 The Magnets 20

3.4 Temperature Control 21

4 Thermometry 23

4.1 General Considerations 23

4.1.1 Considerations in Low Temperature, High 23

Magnetic Field Applications
4.1.2 Thermometry Examples in Low Temperature Physics 24
4.2 Tuning Fork Thermometer 27
4.2.1 Introduction 27
4.2.2 Physical Background 28
4.2.3 Experimental Set-Up 30
4.2.4 Conclusion 42
4.3 Resistance Thermometer 43
4.3.1 Introduction 43
4.3.2 Physical Background 44
4.3.3. Temperature Measurement using RuO_2 and Cernox 45
4.4 Coulomb Blockade Diagram 48
4.4.1 Introduction 48
4.4.2 Physical Background 48
4.4.3 Construction 52
4.4.4 Experimental Set-Up 52
4.4.5 Conclusion 56

5 The Spectrometer 57
5.1 The Spectrometer 59
5.2 Signal Conduction Path 61
5.3 The Switch 63
5.4 Noise Considerations 65

6 NMR Relaxation in Solid Xenon 68
6.1 Introduction 68
6.2 The NMR Coil 69
6.2.1 Coil Design Considerations 69
6.2.2 The Saddle Coil 70
6.2.3 The Probe 73
6.3 Polarisation and Relaxation of Xenon 76
6.3.1 Calculation of Field and Temperature Dependence of Polarisation 79

6.3.2 Temperature and Magnetic Field Dependence of T_1 80
6.3.3 Temperature Dependence of Polarisation 82
6.4 The Relaxation Switch 85
6.4.1 The Oxygen Switch 85
6.4.2 Future Work- The ^{3}He Relaxation Switch 86

7 Discussion 87
7.1 Conclusion 87
7.2 Future work 89

8 Bibliography 90

CHAPTER 1

INTRODUCTION

The possibility of using spin-polarised noble gases, such as ^{3}He and ^{129}Xe to act as a contrast agent and increase the sensitivity in Magnetic Resonance Imaging (MRI) has recently generated wide interest in medical and physics circles. MRI is an imaging technique, which uses magnetic fields and radiofrequency (RF) signals to obtain structural and dynamic information about the matter being imaged. Nuclear Magnetic Resonance (NMR), the phenomenon on which MRI is based (which can be defined as the resonance of nuclei in a magnetic field in response to radiation) is inherently of rather low sensitivity as it depends on a weak, non-ionising radiofrequency (RF) phenomenon. This is because the NMR signal is generated by a very small difference in spin populations aligned parallel or anti-parallel to the applied magnetic field, resulting in the low sensitivity of NMR. In conventional proton MRI, typical polarisation values are of the order of 10^{-4}, whereas spin-polarised noble gases (also called hyperpolarised gases) can increase the magnitude of MRI contrast by 3-5 orders of magnitude [1]. Polarisation of noble gases could be useful in clinical applications as hyperpolarised gases may provide the possibility for non-invasive investigation of human lung ventilation, enabling static imaging while the patient holds his breath or for the study of dynamics of inspiration/expiration and functional imaging**,** which has proven to be difficult for conventional MRI imaging [2]. In the University of Nottingham it is planned to use hyperpolarised ^{129}Xe in lung imaging, perfusion studies, functional MRI and in the study of porous media and catalysts. Bifone et al have tested laser-polarised ^{129}Xe for blood flow imaging [3] with promising results. Mugler et al [4] suggest that both ^{3}He and ^{129}Xe are useful for imaging of gas filled spaces, such as spaces in material or lungs and sinuses in humans and animals.

1.1 Comparison of ^{129}Xe and ^{3}He

Both ^{3}He and ^{129}Xe are non-radioactive, non-toxic, chemically inert and have a spin of $^{1}/_{2}$. ^{129}Xe, which is lipophilic (i.e., it has an affinity for lipids or fat, and therefore binds easily to lipids in the body) is more soluble than ^{3}He in many substances (e.g. blood). Owing to its sensitivity to its chemical environment, it has large chemical shifts (which denotes the change in resonance frequency of a nucleus due to electron shielding), for example even for weak xenon-protein interactions, making it very useful for studying biomolecular structures and interactions [5]. Its non-toxicity makes it useful especially in medical imaging. ^{3}He is rather scarce in nature and has to be produced by the natural decay of tritium. [4]. Xenon is naturally abundant and therefore relatively inexpensive. The isotope ^{129}Xe makes up 26% of natural xenon [6]. It is hoped that the polarised nuclei of ^{129}Xe could transfer their polarisation with protons in the material to be imaged to increase the sensitivity and resolution of proton images. On the other hand ^{3}He has a larger gyromagnetic ratio γ than ^{129}Xe ($\gamma_{3He}=20.38\cdot 10^{7}$ rad T^{-1} s^{-1} and $\gamma_{129Xe}=7.45\cdot 10^{7}$ rad T^{-1} s^{-1}) [6] and therefore a larger magnetic moment and better signal-to-noise ratio, since at constant magnetic field, the signal-to-noise ratio is directly proportional to the gyromagnetic ratio. However, the smaller gyromagnetic ratio of ^{129}Xe may result in less spreading out of the individual fields due to inhomogeneities in the static field B as the resonance frequency $\upsilon=\gamma B_0$.

1.2 Method of Polarisation

The main techniques of polarisation are optical pumping, Stern-Gerlach and brute-force method, all of which are explained in more detail in section 7.3. Polarisation of noble gases has mainly been done by optical pumping, which involves laser treatment of the gas so that the angular momentum from the photons is transferred to the nuclei of the sample gas to produce high polarisation levels. Albert et al [7] optically polarised ^{129}Xe gas and obtained enhanced images of good contrast of the excised lungs of a mouse. The brute-force technique involves the use of high magnetic fields and ultra-low temperatures to achieve polarisation. The high

magnetic fields are required as the polarisation increases with the magnetic field [8]. Solid polarised ^{129}Xe can be stored in the "frozen mode", retaining its polarisation, which facilitates transportation and storage.

1.3 The Relaxation Switch

A major problem that arises is that the spin-lattice relaxation rate T_1 of solid ^{129}Xe increases with magnetic field and increases with temperature, as the low temperature and high field reduce the motion of the particles, which is responsible for relaxation. Honig et al [9] who carried out a feasibility study on polarising ^{129}Xe by brute-force, obtained spin-relaxation times of a few days at a temperature of 1K and moderate magnetic fields without the use of a relaxant. When they increased the magnetic field to 17T at 10mK, the polarisation achieved was 44%, but the relaxation time became too large to measure. The long relaxation times create the need for a mechanism to accelerate relaxation or use a "relaxation switch", which should be easily and quickly removable after inducing relaxation so that the high polarisation level can be retained. One such mechanism is the use of paramagnetic oxygen, which induces relaxation by the coupling of its electronic spin to the nuclear dipoles of xenon. The relaxation inducing capabilities of oxygen in mixture with any sample were mentioned by Bloch [10], who suggests the possibility of establishing first equilibrium of a sample in a strong magnetic field and then evaporating it in an oxygen atmosphere, resulting in very short relaxation times. After removal of oxygen, the polarisation is retained. Honig's experiments showed that condensation of a mixture of ^{129}Xe and oxygen yielded a relaxation time of 5 days at 70mK and 8T with a polarisation of 10%. The aim of this project is to build on Honig's work and achieve a higher polarisation level using stronger magnetic fields and lower temperatures. This necessitates the use of an efficient relaxant, which can be quickly removed or switched off without loss of polarisation.

1.4 Scope of Project

This project investigates the production and relaxation of spin-polarised condensed, solid ^{129}Xe using brute-force polarisation at high magnetic fields of maximum 15T and low temperatures ranging from about 10 millikelvin to a few Kelvin. The NMR signal of the solid ^{129}Xe sample, containing oxygen, has been measured and the temperature and field dependence of the NMR signal and the spin lattice relaxation time T_1 of the xenon sample, into which oxygen is introduced as relaxant, have been evaluated. The experimental polarisation and relaxation results obtained are compared with the calculated values. The feasibility of accelerating the relaxation rate by oxygen and its removal without loss of polarisation is studied and the alternative of using ^{3}He as relaxant is proposed. The equipment required to achieve this aim is described in this report.

Chapter two deals with the principles of NMR underlying this project.

The ^{3}He-^{4}He dilution refrigerator used to cool the sample to millikelvin temperatures and the system used to apply the static magnetic field are explained in Chapter three, which also describes briefly the methodology and software programs used to maintain and control the temperature to ensure reliable NMR measurements.

The accurate measurement of temperature is complicated by the need for a thermometer, which works reliably at ultra-low temperatures and high magnetic fields. To this effect the tuning fork thermometer was devised and tested, which is discussed in Chapter four along with resistance thermometry and the Coulomb Blockade Thermometer.

Chapter five deals with the spectrometer, software and the coupling circuits used in NMR spectroscopy. The Spectrometer transmits RF (radiofrequency) pulses (according to a pulse sequence generated by a Labview program we wrote) through the coupling circuits and the coil to the sample. The NMR signal is picked up by the same coil and passed through coupling circuits to the receiver of the spectrometer

and finally displayed on the monitor screen for evaluation using the same Labview program.

Chapter six gives a detailed description and analysis of the polarisation method, the NMR experiments, and the polarisation and relaxation results obtained. The coil, which transmits the RF pulse into the sample and picks up the induced NMR signal, is described. Finally, a treatment of the feasibility of the oxygen switch as relaxant and the proposition to use ^{3}He as relaxant is given.

The results of the project are summarised in chapter seven. All references used in any form are listed in the bibliography in chapter eight.

CHAPTER 2
PRINCIPLES OF NUCLEAR MAGNETIC RESONANCE

The phenomenon of *Nuclear Magnetic Resonance (NMR)* has been widely used to study the structure and dynamics of nuclear spin systems in physics and chemistry. Nuclear *Magnetic Resonance Imaging (MRI)* has also emerged as a powerful imaging technique, popular in the medical field as it is non-invasive and uses non-ionising radiation, traditionally used to image liquid in spaces such as the lungs or blood flow, but its scope is extended continuously, e.g. to image the abdominal area and brain. The principles of NMR are explained briefly in the next section. The main sources of material used to explain NMR are given in references [11] to [14] or as mentioned in the text.

2.1 Method Of Magnetic Resonance

Bloch defines the method of magnetic resonance as: "*The observation of transitions caused by resonance of an applied radiofrequency field with the Larmor precession of the moments around a constant magnetic field*". [10]

Magnetic Resonance arises due to the spin and magnetic moment possessed by certain nuclei of a system, having an odd number of protons and/or neutrons. Apart from orbiting around the nuclear axis, they also spin about their own axis. The nuclear angular momentum L, called spin and written as $L=hI$, where h is Planck's

constant and *I* is the spin quantum number, is related to the nuclear magnetic moment μ by

$$\mu=\gamma L \qquad (2.1)$$

where γ, the *gyromagnetic ratio,* is a constant, characteristic of a specific nucleus.

When an external static magnetic field of strength B_0 is applied to a sample, the magnetic moments align themselves parallel or anti-parallel with the field, with a slight excess of parallel nuclei, resulting in a net magnetic moment M_0. The torque acting on the nuclear dipoles in the field results in precession, or wobbling, of the magnetic moment around the magnetic field at a particular frequency called the *Larmor frequency* ω, which depends on the gyromagnetic ratio γ and the static applied magnetic field strength B_o.

$$\omega=\gamma B_o \qquad (2.2)$$

The proof of this theorem, called *Larmor theorem,* can be found in reference [11]. The other important event that occurs is the splitting of the energy of the nuclei into two energy levels. The higher energy level corresponds to the magnetic moments aligned in parallel with the field and the lower level corresponds to the magnetic moments aligned in anti-parallel with the field. To excite a nucleus from the lower to the higher energy level, energy at the Larmor frequency has to be supplied, i.e.

$$E=h\upsilon \qquad (2.3)$$

The net magnetisation M_0 is considered to be along the Z-axis in a three-dimensional co-ordinate system by convention. To measure the NMR signal the magnetisation has to be flipped into the XY plane. This is done by applying a second magnetic field or an RF pulse at the Larmor frequency to the sample, which rotates the magnetisation vector by an angle, whose degree value depends on both the amplitude and length of the RF pulse. The frequency of the magnetic moment in the XY plane (*M)* is still the Larmor frequency. Off-equilibrium values of the magnetisation along

the Z-axis are denoted by M_Z. When the RF pulse is turned off, this magnetisation decays towards the Z-axis and equilibrium position. Nuclei in the higher unstable energy level come down to the lower energy state after a certain amount of time, emitting electromagnetic radiation at the Larmor frequency, which decays exponentially and is called *Free Induction Decay (FID)*, shown in figure 2.1.1. The FID signal induces the NMR signal in the receiver coil placed near the sample, which decays exponentially according to:

$$A = A_0 \exp\left(-t / T_2^*\right) \qquad (2.4)$$

Where A is the amplitude of the FID at time t, A_0 is the initial amplitude and T_2^* is the average decay time for the process, also known as spin-spin relaxation time (including the effect of field inhomogeneities), explained in section 2.2. The measured FID gives an indication of the number and type of nuclei present in the sample.

A brief summary of the NMR detection system is as follows. The sample is subjected to a static magnetic field B_0. An RF pulse is applied through the RF transmitter by the coil wound around the sample, whose magnetic field B_1 is perpendicular to the static field. This tips the magnetization into the XY plane. After the RF pulse is turned off, the magnetisation returns to its equilibrium state, inducing a voltage in the receiver coil resulting in the FID signal.

Fourier Spectrum of the NMR Signal

The magnitude of the FID signal is measured as a function of time, which makes interpreting it sometimes inconvenient. Using Fourier transformation the FID signal in the time domain can be transformed into the frequency domain as can be seen in figure 2.1.1. A number of FID's may be averaged to improve the signal-to-noise-ratio, and then Fourier transformed to obtain the signal in the frequency domain.

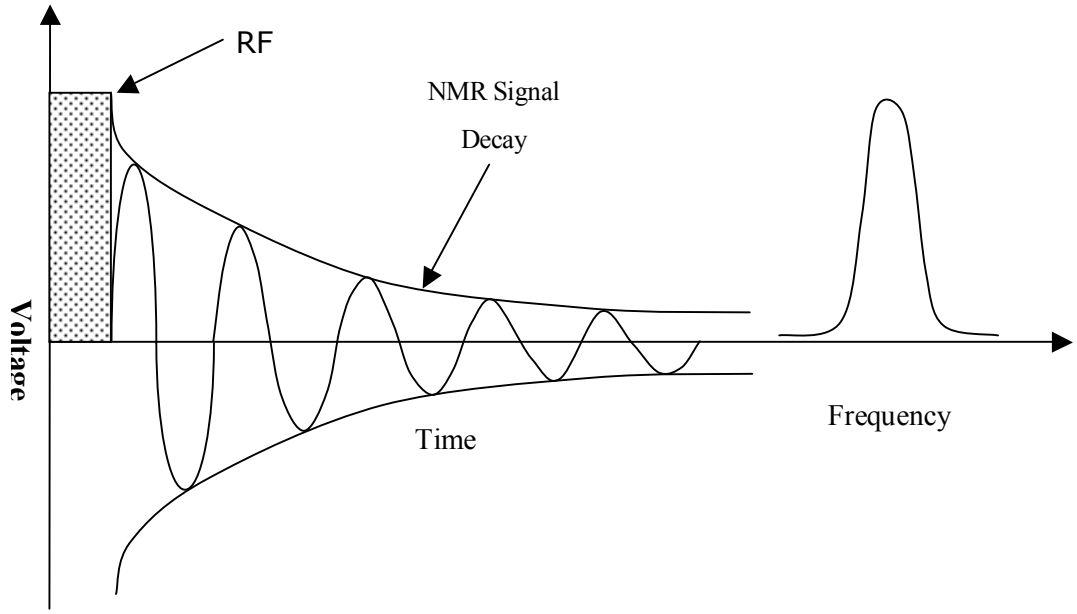

Figure 2.1.1: Free Induction Decay after application of RF pulse shown in time domain and frequency domain.

The Rotating Frame Of Reference

When the RF pulse at Larmor frequency is applied to the nuclear system in the static magnetic field B_0, M_Z is tilted from the Z-axis into the XY plane (*M)*, where it precesses at Larmor frequency. The laboratory frame of reference of this process is shown in figure 2.1.2. The more suitable and conventionally used technique of the rotating frame of reference of the same process is shown in figure 2.1.3. Here the magnetisation remains stationary with respect to the rotating frame of reference describing its motion.

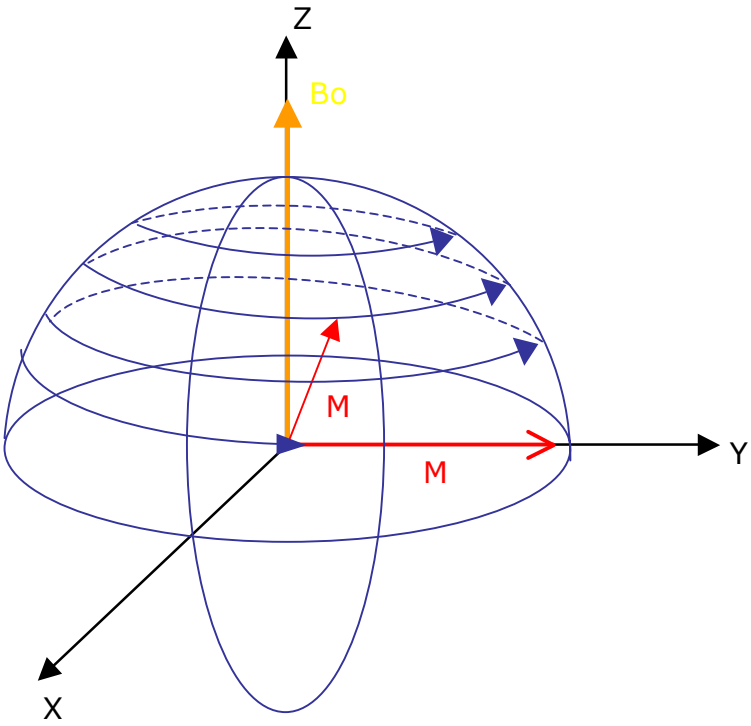

Figure 2.1.2: Laboratory frame of reference showing precession of magnetization *M* in XY plane in static field B_o after application of RF pulse [13].

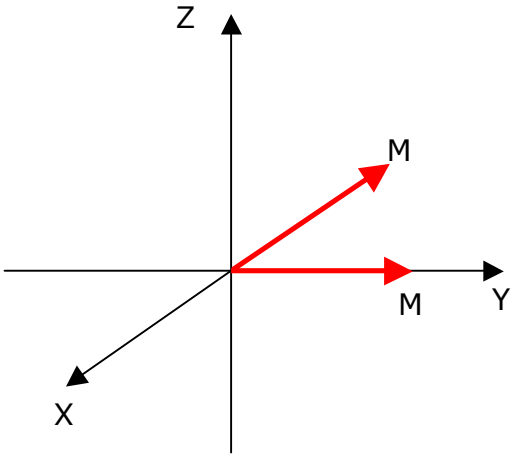

Figure 2.1.3: Laboratory frame of reference showing precession of magnetization *M* in XY plane in static field B_o after application of RF pulse [13]

2.2 Relaxation Times

Subjecting a sample to an RF pulse shifts it away from equilibrium by introducing energy into the system, causing the magnetisation vector to precess in the XY plane. At equilibrium the magnetisation vector of magnitude M_o is aligned along the z-axis and there is no coherent magnetisation in the XY plane. There are two types of relaxation: Spin-lattice relaxation denotes the return of the magnetisation vector along the z-axis to its original value M_0 and spin-spin relaxation denotes the loss of coherent magnetisation in the XY plane. The rates at which these relaxation processes are described by two time constants: T_1 is the spin-lattice relaxation time and T_2 is the spin-spin relaxation time. The relaxation rates depend on several variables, like the temperature, magnetic field and structure and therefore their measurement can provide useful information about the sample. They are measured by combinations of RF pulses and magnetic field, described in the next section, such as "progressive saturation" and "inversion recovery" to measure T_1, and "spin echo" to measure T_2.

2.2.1 Spin-lattice Relaxation

As already mentioned, spin-lattice relaxation occurs by the spin system losing energy to the surrounding lattice when the excited nuclei return to the ground state by transferring their energy to surrounding particles during collisions, causing the magnetisation vector of the system, M_z, to return to its equilibrium position M_0. As this process does not happen spontaneously, the energy emission has to be stimulated. If the frequency of the magnetic field generated by the random movement of the charged particles is at the Larmor frequency, transitions between the excited and ground state can occur. The rate at which energy is transferred between the nuclei and the surrounding lattice depends on the amount of their motion. The rapid movement of particles in a liquid facilitates energy redistribution and therefore the T_1 of liquids is generally shorter than that of solids. The T_1 also depends on the temperature as thermal excitation increases the motion of molecules. Spin-lattice relaxation can be described mathematically using the Bloch equation.

$$\frac{dM_Z}{dt} = \frac{(M_0 - M_Z)}{T_1}$$

$$M_Z = M_0\left(1 - e^{\frac{t}{T_1}}\right) \qquad (2.5)$$

2.2.2 Spin-Spin Relaxation

Spin-spin relaxation occurs by the system losing coherent magnetisation in the XY plane by interactions of nuclear spins. The energy emitted by nuclei when they return from higher to lower energy states can be absorbed by other nuclei, resulting in the mixing of spin populations, which leads to signal incoherence. Considering the rotating frame of reference, mathematically T_2 can be described using:

$$\frac{dM_{xy}}{dt} = \frac{-M_{xy}}{T_2^*}$$

or

$$M_{xy} = M_0 \exp\left(\frac{-t}{T_2^*}\right) \qquad (2.6)$$

A problem in measuring T_2 arises as loss of coherence can also be induced by field inhomogeneity. To find the true T_2, this effect has to be eliminated, which can be done by the spin-echo procedure. In equation *(1.6)* T_2^* denotes the spin-spin lattice relaxation time taking into consideration the effects due to field inhomogeneity.

2.3 Pulse Sequences

Different pulse sequences are used to measure specific parameters, such as T_1 and T_2, put together using magnetic field gradients and RF pulses. As mentioned before, the most common pulse sequences used to measure T_1 and T_2 are *saturation recovery* and *inversion recovery* to measure T_1 and *spin-echo* to measure T_2.

2.3.1 Saturation Recovery

This pulse sequence consists of a number of 90˚ pulses separated by a time delay τ, which should be longer than the spin-lattice relaxation time T_1 to give the magnetisation M_Z sufficient time to recover to its equilibrium value along the Z-axis. After the application of 4-5 RF pulses equilibrium is achieved between the energy introduced by the RF pulses and the loss of energy through spin-lattice relaxation. The magnitude of the FID is directly proportional to M_z. τ is adjusted to sensitise the procedure to the T_1 of the sample. In this study, from the very long T_1*'s* we monitor the growth of the polarisation by producing FID's following very small tipping pulses.

2.3.2 Inversion Recovery

The inversion recovery pulse sequence, mainly used for T_1 measurement, consists of a 180˚ pulse followed by a delay period, then a 90˚ pulse, an acquisition period and another delay period. The 180˚ pulse flips the magnetisation onto the opposite axis, in this case, the z-axis, resulting in a total inversion of the populations of the energy levels. The magnetisation along the positive Z-axis recovers during the delay period τ. The 90˚ pulse rotates the magnetisation into the XY plane and the magnitude and orientation of the FID is measured in the next delay time. The long time delays of the order of 3-5 times the T_1 for complete relaxation make this method very time consuming and therefore not suitable for this study as T_1 is already very long at the

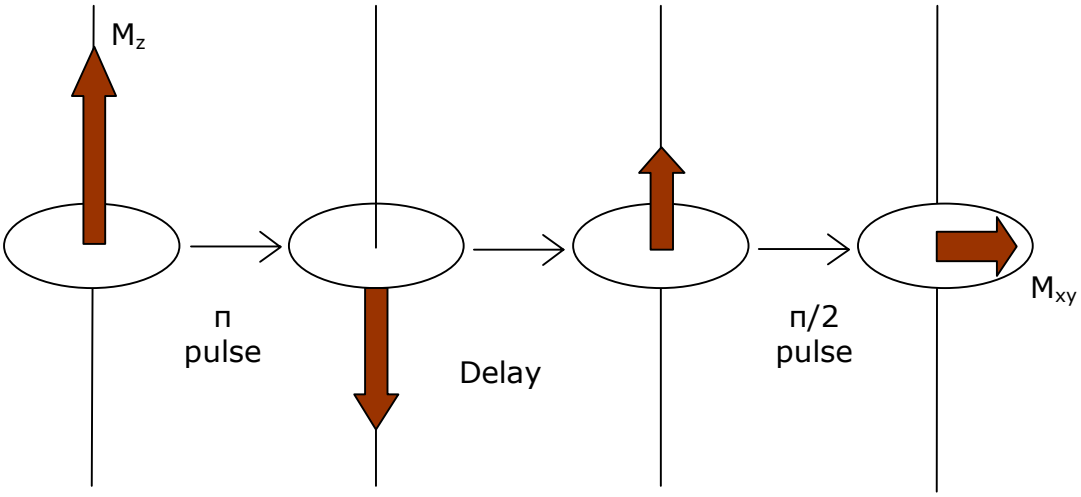

Figure 2.3.1: Inversion Recovery pulse sequence

low temperatures and high fields used. The pulse sequence for the inversion recovery experiments is shown in figure 2.3.1.

2.3.4 Spin Echo

This pulse sequence is used in T_2 measurements to differentiate between the intrinsic T_2 and the T_2 caused by the magnetic field inhomogeneity. It consists of a 90˚ pulse, delay period τ, 180˚ pulse, and another delay period τ and acquisition period. Here the magnetisation is first flipped onto the X-axis. Because of the inhomogeneity of the magnetic field, the nuclei precess at different rates, resulting in the spreading out of the individual magnetisation vectors around the X-axis, leading to phase incoherence of the magnetisation. The 180˚ pulse flips these individual components onto the negative X-axis in the rotating frame, where they are spread out in the same manner and therefore cancel each other resulting in coherent magnetisation, which can be measured during the acquisition period. This pulse sequence is shown in figure 3.2.2.

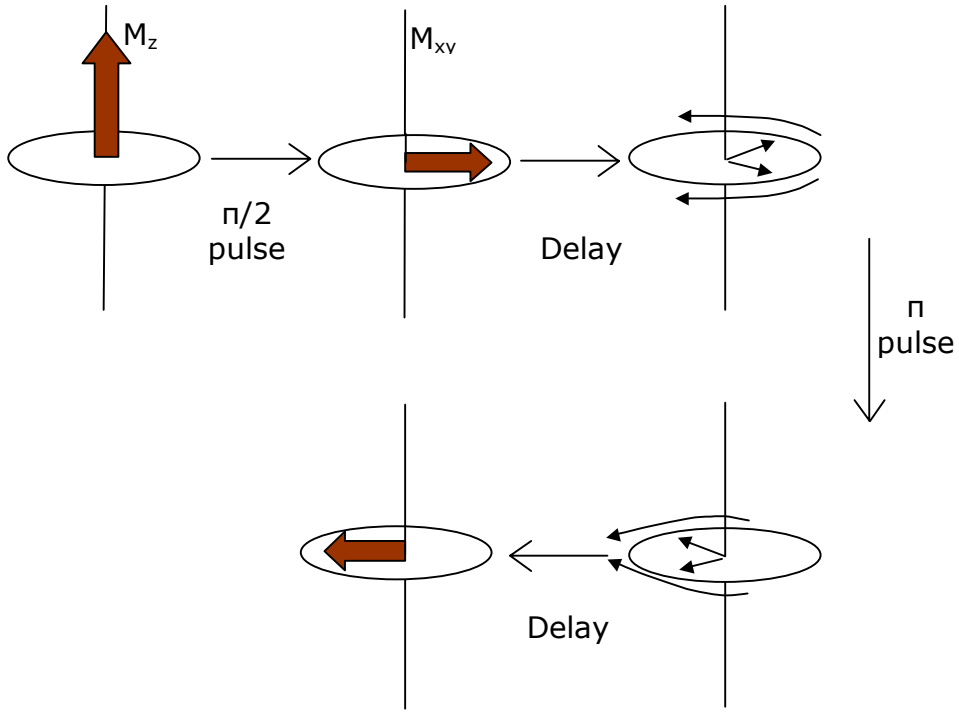

Figure 2.3.2: Spin echo pulse sequence

2.4 Chemical Shift

Chemical shift is the change in the resonance frequency of nuclei due to the electrons surrounding it. The motion of the electrons creates magnetic fields, which oppose the static applied magnetic field B_0. This results in a decrease of the total magnetic field, which in turn changes the resonance frequency. This property is useful to identify substances as the nuclei, which occupy different chemical environments (and therefore are subjected to different electronic charge distributions), precess at different frequencies. As mentioned in the introduction, it turns out that ^{129}Xe has a particularly high chemical shift when dissolved in certain substances, which is a very important and useful property in imaging.

CHAPTER 3
THE ^{3}HE-^{4}HE DILUTION REFRIGERATOR

The dilution refrigerator is used to carry out cooling continuously at temperatures below 0.3K. For this project, we used an Oxford Instruments top-loading ^{3}He-^{4}He dilution refrigerator, model Kelvinox TLM, which provides a cooling power of more than 250μW at 100mK, has a base temperature of below 15mK and a maximum temperature of 300K [16]. The probe can be inserted directly into the helium mixture inside the mixing chamber. The lowest temperature that we could cool down till now was about 10mK.

3.1 Principle of Operation

The dilution refrigerator operates by diluting liquid ^{3}He in ^{4}He.

As shown in figure 3.1 [15], the area below the phase separation line shows the region in which ^{3}He and ^{4}He are not miscible. So if the temperature of the mixture is below the phase separation line, at the concentrations shown, ^{3}He and ^{4}He separate into two phases. The lower phase is rich in ^{4}He and the upper phase is rich in ^{3}He, which preferably rises to the top because of the lower density of ^{3}He. So the two phases are maintained in liquid-vapour form. Since there is a boundary between both phases, extra energy is required for the ^{3}He atoms to go from one phase to another. This energy is obtained from the walls of the chamber containing the phases in the form of heat.

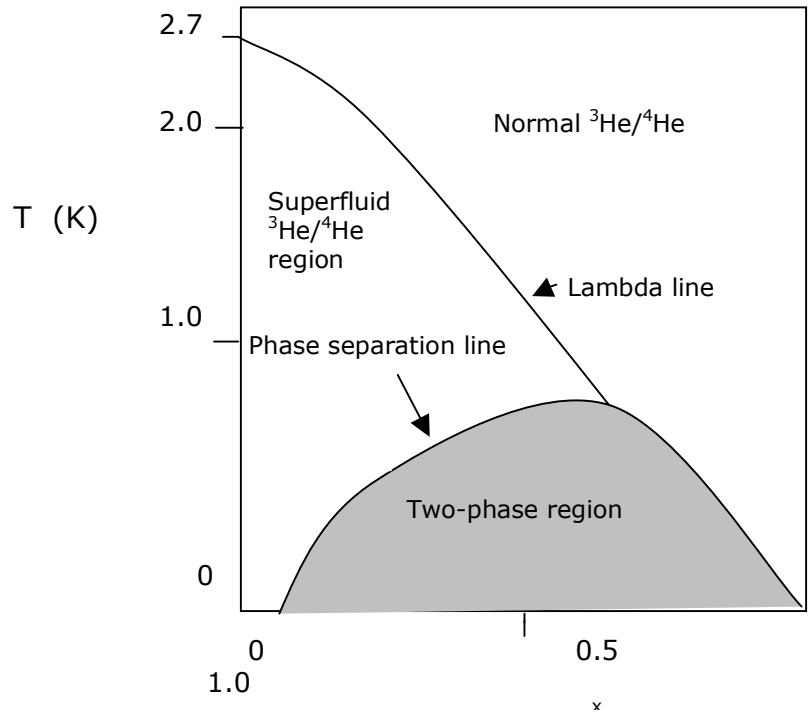

Figure 3.1: Phase separation of liquid ^{3}He-^{4}He mixture at saturated vapour pressure. X denotes the ^{3}He concentration in the mixture and T is the temperature in Kelvin. (For details see text)

As the walls are in contact with the sample space, this lowers the temperature of the sample. Close to absolute zero temperatures the ^{3}He rich phase becomes almost pure, but its concentration in the lower ^{3}He gas phase still remains finite. This ensures that ^{3}He transfer of atoms from the upper into the lower layer can take place at any temperature.

Figure 3.2 [16] shows a schematic diagram of the inner vacuum chamber of the dilution refrigerator, which is immersed in liquid ^{4}He. The pumps ensure continuous circulation of ^{3}He and ^{4}He from the storage dumps into the 1 Kelvin pot (1K pot) to the mixing chamber where eventually the phase separation takes place and back to the dumps through the still. When the refrigerator is started,
the ^{3}He-^{4}He mixture, coming from the storage dumps is condensed in the 1K pot to 1.2 K. When the vapour pressure in the still is reduced, the temperature is further lowered to 0.86K at which point phase separation takes place in the mixing chamber.

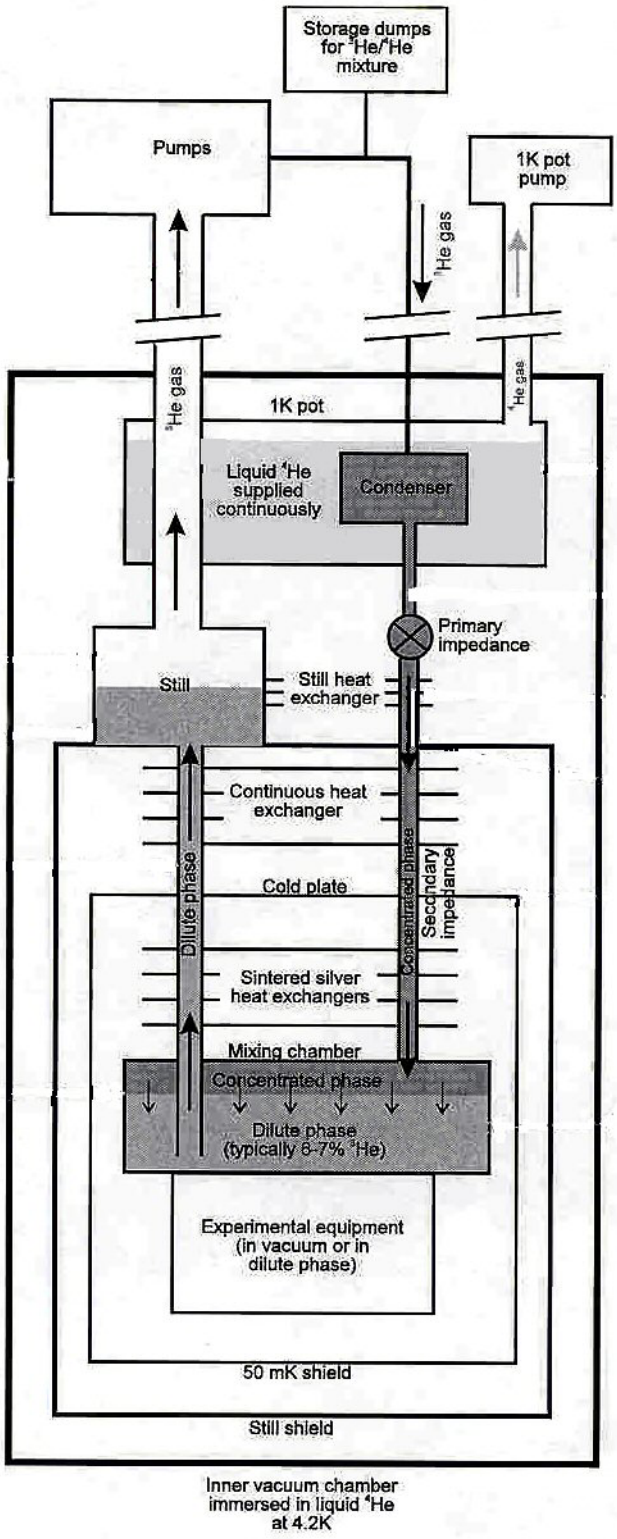

Figure 3.2: Inner Vacuum Chamber of Dilution Refrigerator [16].

The ^{3}He expands into the lower phase, thereby causing cooling as explained above. To ensure that the dilute phase does not become saturated with ^{3}He, the temperature is slightly raised and therefore the pressure of ^{3}He becomes larger than that of ^{4}He and it evaporates into the concentrated phase. As the pressure of ^{3}He in the still is lower than in the mixing chamber, the mixture from the lower phase moves to the still and cools the returning flow of ^{3}He through a number of heat exchangers. The continuous heat exchangers consist of tubular coils and are used for temperatures above 50 mK. The sinted silver heat exchangers increase the contact area of the walls with the liquid in the mixing chamber to provide efficient heating of the sample at very low temperatures, when the resistance between walls and liquid increase. From the still ^{3}He is pumped out, compressed, filtered and then returned to the Helium bath to re-enter the flow into the 1K pot.

3.2 Cooling Procedure

Before running the refrigerator it had to be leak tested, to ensure effective use of the expensive ^{3}He liquid and to avoid safety hazards, using a mass spectrometer leak detector. The Helium reservoir was pre-cooled to 77K using liquid Nitrogen. When the temperature of the system reached 77K, the liquid nitrogen was pumped out again. The next step was to cool down the system to 4.2K. First the inner vacuum chamber (IVC) was flushed with Helium exchange gas and then liquid Helium was admitted into the Helium reservoir through a siphon tube using a hand or foot bladder to exert slight pressure and speed up the process. Care had to be taken not to do this too quickly, so as to avoid excessive ^{4}He boiling off as Helium liquid has a very low latent heat of evaporation but high enthalpy. After pre-cooling the system to 4.2K it was ready for use. The dilution refrigerator is controlled by a software called Object Bench, provided by Oxford Instruments, which ensures that after the system has reached 4.2K, the helium mixture fills the 1 K pot, condenses and enters the cooling cycle inside the mixing chamber as explained in section 3.1.

3.3 The Magnets

There are two superconducting magnet stages. The top magnet has a field strength B of 4.5T and the bottom magnet, which surrounds the sample space, of 15.5T. Figure 3.3 shows the variation of the magnetic field with the distance along the probe. There are compensation coils (which allow small shifts of the main field) and shim coils (which remove residual gradients and hence improve homogeneity of the field included. The magnet system is fitted with superconducting switches in parallel with its windings, which allows the magnets to be operated in persistent mode. In this mode the superconducting circuit constitutes a closed loop and the magnets provide a stable field even when the power supply is switched off. We used two types of power supplies. One was an Oxford Instruments 120A power supply used with the main magnet and the other one was a 5V power supply for the heater, which sent current through the magnet to keep it in the normal state. During energisation of the magnet, a small amount of current (about 50mA) is supplied to the switch to bring it to the normal state. As its resistance in the normal state is much higher than that of the main winding of the magnet, the current preferably flows through the magnet. When the power supply to the heater is stopped the switch closes and allows current flow, thereby gradually reducing the current in the magnet leads till the switch carries the full current. To de-energise the magnet, the switch heater is turned on and its power gradually increased. Due to the finite resistance of the switch, current starts flowing through the magnet resulting in de-energisation.

For our purposes a problem encountered was that the magnets interacted with each other, thereby changing the fields, changing the resonance frequency ω_0. As it was not possible to quantify in exact mathematical terms how the fields affected each other, we found the fields required by both magnets to give the necessary field strength using trial and error method. This was done by varying the field strengths of the magnets and measuring each time the resulting NMR signals using the spectrometer. Also the static magnetic field B_0 decays slowly in time. According to this decay, ω_0 had to be shifted to keep on resonance.

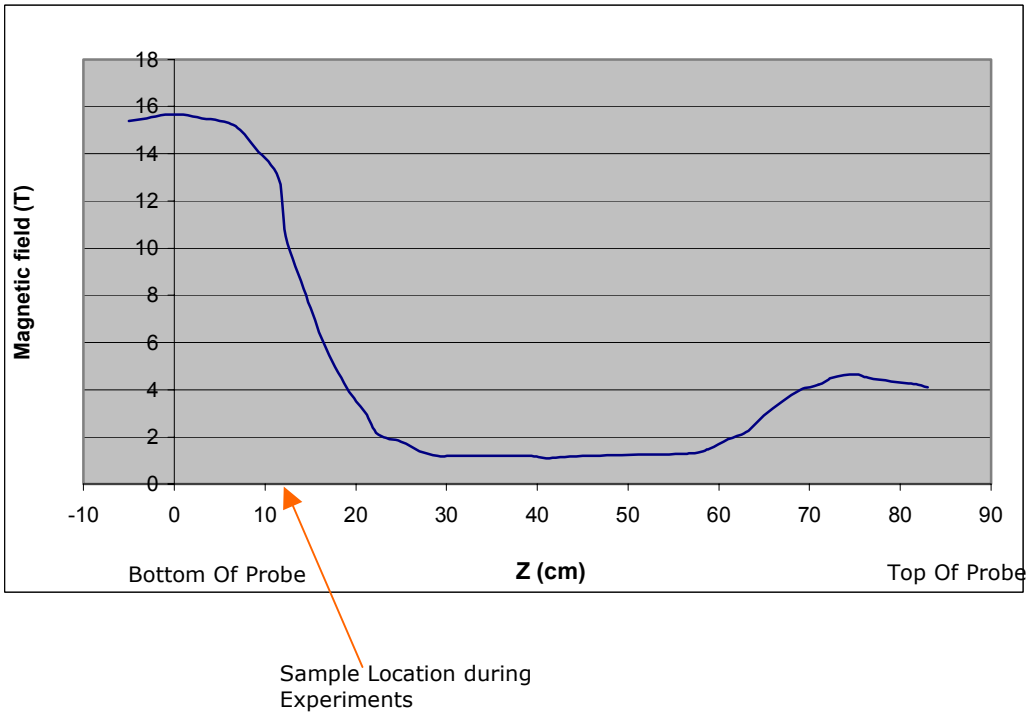

Figure 3.3: Graph showing variation of magnetic field B (T) with distance from bottom of the probe Z (cm).

3.4 Temperature Control

Owing to the significant temperature dependence of polarisation of the sample, it is vital to keep the temperature of the dilution refrigerator stable. This is done by adjusting the power supply of the heater inside the mixing chamber till it balances the cooling power of the refrigerator. It is also possible to achieve gradual cooling of the refrigerator in the preferred time by changing the power supplied to the heater. To regulate the temperature we used an *AVS-47 ac resistance bridge*, which measures the resistance inside the mixing chamber using a resistance thermometer. This resistance is converted programmatically to the corresponding temperature and fed into the *TS-530 temperature controller*, which controls the power supply of the heater. Labview programs are used to monitor and control these procedures. The mixing chamber of the dilution refrigerator contains a thermometer. Figure 3.3 shows how the components of the temperature control system are related.

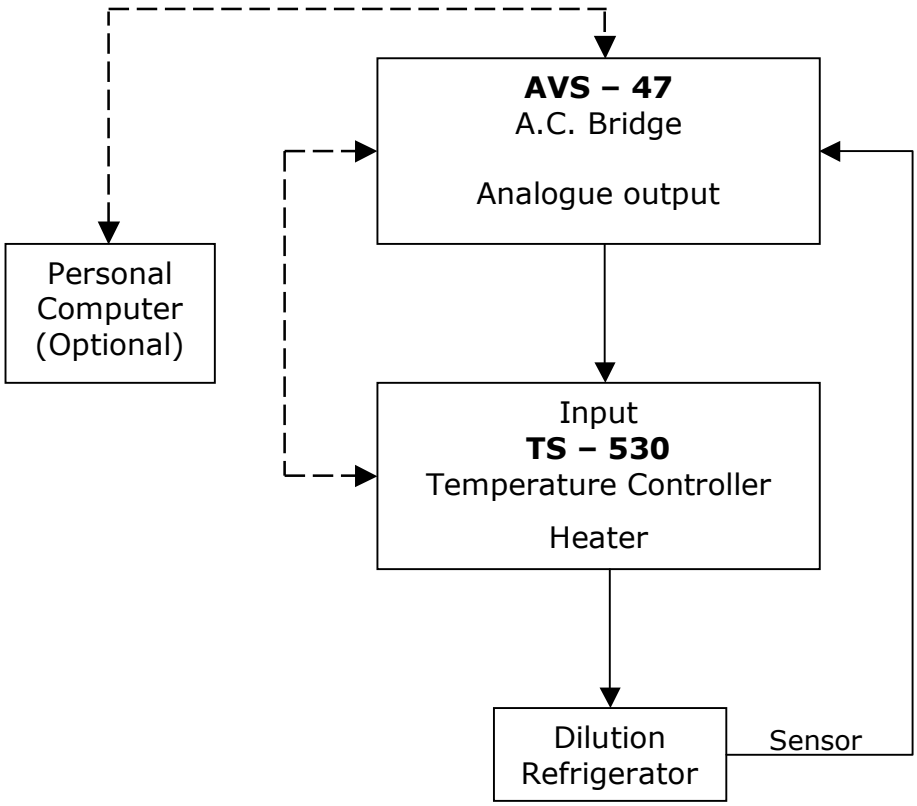

Figure 3.3: Schematic diagram of temperature control cycle.

A photograph of the gas handling system, which was used to transfer gases around by means of a pumps is shown in figure 3.4, showing the gas terminals which can be opened and closed by means of valves. Figure 3.5 shows a photograph of the Kelvinox Intelligent Gas Handling System Control [33]. The gas paths and valves indicators can be seen on the front panel of the system.

Figure 3.4: Photograph showing gas-handling system

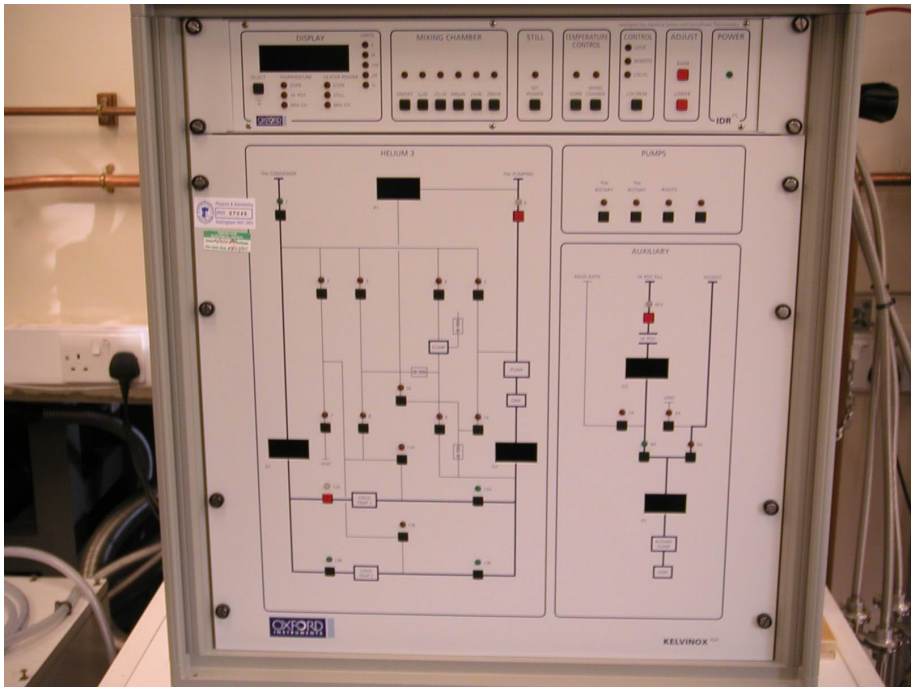

Figure 3.5: Photograph showing Kelvinox Intelligent Gas-Handling System Controller [33]

CHAPTER 4
THERMOMETRY

4.1 General Considerations

The accurate determination of the temperature of our sample is a crucial part of our project. The boiling point of helium is 4.2K and that of Xenon is 165K. We plan to achieve hyperpolarisation of solid xenon in the millikelvin temperature range with high magnetic fields applied. The experiments take place in a temperature range of about 18mK to 10K and magnetic fields of about 15 T. These conditions impose several difficulties in measuring the temperature. Conventional thermometers do not function at ultra low temperatures or are affected by magnetic fields. Following are the thermometry conditions that have to be met for our specific purposes.

4.1.1 Considerations in Low Temperature, High Magnetic Field Applications

Besides the constraints imposed by the low temperature and high field conditions, there are other requirements that need to be considered. Thermometers can be categorised into two types [17]: The primary thermometer, which gives the temperature with reference to an absolute temperature scale and the secondary thermometer, which has to be calibrated against the primary thermometer. Secondary thermometers might be more sensitive or more convenient for specific purposes but their reproducibility is limited and so sometimes they may need to be calibrated during every run. It is vital to make sure that the thermometer is in thermal contact with the sample whose temperature has to be measured and not affected by other

sources of heat. In the ^{3}He-^{4}He dilution refrigerator used, care had to be taken that the thermometers were placed as far away from the heater inside the mixing chamber as possible. It is essential that the interconnecting leads of the temperature-measuring device do not transfer excessive amounts of heat to the sample. Joule heating of the leads becomes more dominant at lower temperatures. Therefore, the signal amplitude should be reduced as the temperature reduces. In addition methods to provide heat sinking could be useful.

4.1.2 Thermometry Examples in Low Temperature Physics

Resistance thermometers

Resistance thermometers are based on the temperature dependence of the resistance of a metal or semiconductor. Sensitivity down to 20mK is achievable, depending on the material. They are convenient because of their linearity but the demerit is that most resistance thermometers exhibit magnetic field dependence. A frequently used pure metal in resistance thermometers is platinum, which gives high accuracy and sensitivity above 30K; at lower temperatures, its field dependence increases. Semiconductor thermometers are used as secondary thermometers in the temperature range between 10mk and 10K. Theoretically their resistance R varies with temperature T as [15]:

$$R(T) = \alpha \exp(\frac{\Delta E}{2K_B T})$$

where α denotes the temperature-dependent mobility of charge carriers, ΔE is the energy gap between conductance and valence bands and k_B is Boltzman's constant. They are unsuitable for temperature measurements below 1K as their resistance becomes too high to measure at that temperature. An exception is the Ruthenium Oxide (RuO_2) thermometer, whose temperature dependence is given by [15]

$$R(T) = R_0 e^{\left(\frac{T_0}{T}\right)^{0.345}}$$

in a temperature range of $35 \leq T \leq 800mK$, giving a 2% fit. They can measure temperatures from 4.2K to 25mK and exhibit little field dependence. Other advantages are their small size, low weight (of a few milligram), low cost and the reproducibility of their behaviour after thermal cycling. Cernox (Ceramic Oxynitride) thermometers, manufactured by Oxford Instruments [16], too show high field independence but their temperature range is very limited and we could not measure temperatures below 1.4K. Details of the Cernox and RuO_2 thermometers, which we tested down to 18mK, are discussed in section 4.3.

Capacitance Thermometers

Capacitance thermometers give an indication of the temperature, as the dielectric permittivity ε is proportional to the temperature *T*. In amorphous substances, a dependence of $\varepsilon \propto -ln\ T$ is followed [17]. This concept is very useful if the dielectric constant of the sample itself changes with temperature. They can be used to measure temperatures in a range of 1K to 1mK. Compared to resistance thermometers they are more accurate and exhibit less self-heating. They are unaffected by magnetic fields up to 20T [15]. They have a fast response and good resolution (10μK at 1mK). Their disadvantage is that they require a capacitance bridge and may suffer drift after temperature changes [18].

^{3}He Melting-Curve Thermometer

These are based on the temperature dependence of the melting pressure of ^{3}He. They measure temperatures in a range of 0.3K to 2mK. Greywall [19] conducted experiments on the specific heat of pure ^{3}He in both the fluid and superfluid state between 0.6K and 5mK. He related the pressure *P* and temperature *T* using a simple polynomial fit:

$$P - P_A = \sum_{i=-3}^{5} a_n T^n$$

where P_A=34.3389 bar, is the pressure at which ^{3}He fluid becomes superfluid, i.e. its viscosity vanishes or it flows without inner friction. The coefficients of *a* are given in Greywall's findings. This method is field independent, has a very high resolution (1μK) and reproducibility and almost no power dissipation. Its disadvantage is that it is difficult to calibrate and has a slow response due to its large heat capacity.

Vibrating wire resonators

The vibrating wire resonator uses the fact that the viscosity of liquid ^{3}He varies as T^{-2} from a few 100mK down to a few mK. The viscosity is given by the width of the line of the mechanical resonance of a wire placed in a magnetic field and excited with an ac current. Vibrating wire resonators have been widely used to measure temperatures in ^{3}He and ^{3}He-^{4}He mixtures. Their useful temperature range is from 50mK to 100μK [20]. Obtaining a high quality factor is difficult with this method, as it involves increasing the diameter of the wire or the density, which in turn would increase eddy current damping.

We use the simple and cheap alternative to vibrating wire resonators: tuning forks. The other methods we found convenient for our purposes are the RuO_2 and Cernox resistance thermometers and the Coulomb Blockade Thermometer.

Tuning Fork Thermometer

Quartz crystal tuning forks operate by the principle of the piezoelectric effect, i.e. subjecting them to a mechanical force induces a voltage and vice versa. Their resonance frequency and quality factor depends on the viscosity of the medium, which in turn depends on the temperature. We have tested them in temperatures ranging from room temperature to 18mK in different media such as vacuum, air and Helium gas. The main advantage is their easy and inexpensive set-up. They are independent of the magnetic field and have high values of Q. (up to 50 000 in vacuum). Details of our experiments and the results are given in section 4.2.

Coulomb Blockade Thermometer

The Coulomb Blockade Thermometer (CBT), based on the Coulomb blockade, measures the conductance drop across a series of tunnel junctions. The CBT is commercially available from Nanoway [21]. Its ideal temperature range is from 20mK to 1K. It is independent of the magnetic field; its main drawback is the lower temperature limit.

4.2 TUNING FORK THERMOMETER

4.2.1 Introduction

A novel concept that the low temperature group of University of Nottingham has devised is tuning fork thermometry, which is based on the change of tuning fork parameters such as the resonant frequency (f_R) or quality factor (Q) with temperature. Clubb [22] investigated the use of tuning forks in low temperature viscometry in solutions of pure ^{3}He and different concentrations of ^{3}He-^{4}He mixtures as an alternative to vibrating wire viscometry. He has shown experimentally that the tuning fork behaviour is field independent in magnetic fields up to 10T. Tuning forks have already found wide use in microscopy such as scanning near field optical or acoustic microscopy, scanning force microscopy, magnetic force microscopy etc. Rychen et al [23] studied their suitability as force sensors in a cryogenic environment down to a temperature of 1.5K and in magnetic fields up to 8T.

To determine the suitability of tuning forks for thermometry in our project we examined the variation of the properties of a tuning in a temperature range from 18mK to room temperature in different media and subject to different pressures. We used a method similar to Grober *et al* [24]. The tuning fork was driven electrically and the admittance and phase measured by the lock-in amplifier was used to calculate the tuning fork resonant frequency and quality factor. The data we measured showed dependence of tuning fork parameters on the temperature and very low or very high pressures. We used commercially available tuning forks, which have a vacuum resonant frequency of 32768Hz (2^{15}Hz). Owing to their magnetic field independence, the high values of the quality factor, easy set-up and cheapness (about £0.20 per tuning fork) we found them to be very convenient for low temperature, high field applications.

4.2.2 Physical Background [25] [26]

The temperature dependence of the resonant frequency and quality factor of the tuning fork depends mostly on the viscosity of the medium in which it is immersed, which we expect to vary with temperature *T*. Viscosity can be explained as follows: The layers of a liquid exert a force on the underlying layers thereby transferring momentum between layers. Considering two layers, this force *F* is proportional to the area of the surfaces *A*, the difference in their velocity, $\Delta u = u_{\text{top-layer}} - u_{\text{bottom-layer}}$, and inversely proportional to the distance Δz between them.

$$\frac{F}{A} \propto \frac{\Delta u}{\Delta z} \qquad (4.2.1)$$

The constant of proportionality is a called co-efficient of viscosity η.

$$\frac{F}{A} = \eta \frac{du}{dz} \qquad (4.2.2)$$

The temperature dependence differs for liquids and gases. In liquids, friction between fluid layers originates from molecules sliding past each other. For a liquid the viscosity decreases as the temperature increases because the higher kinetic energies at higher temperatures in a liquid overcome the attractive forces of the molecules and allow them to slip past one another with greater ease. The more viscous the liquid is the larger is the change in viscosity with change in temperature. In gases, molecular collisions transfer momentum between layers. For a classical gas the viscosity increases with increasing temperature in proportion to $\sqrt{T}$ because as temperature increases, the molecules move faster and more momentum is transferred between layers, which increases the viscosity.

Using equation *4.2.2, t*he coefficient of viscosity η is given by:

$$\eta = \tfrac{1}{3} \rho c l \qquad (4.2.3)$$

Where ρ is the mass, per unit volume, c is the mean thermal velocity and l is the mean free path, which is the average distance travelled by an atom before collision with another atom takes place. The factor 1/3 arises due do geometrical factors, which influence the viscosity. The mean free path influences the rate of viscosity. In a dilute gas a molecule can pass in between the other molecules without hitting them so the mean free path is larger than the average distance between molecules. If n is the number of particles per unit volume and σ the cross-sectional area of the atom, then the mean free path l is given by:

$$l = 1/\sqrt{2}n\sigma \qquad (4.2.4)$$

For a gas the viscosity is independent of pressure because as the rate of momentum transferring collisions decreases with decreasing pressure, the distance between the particles increases. This in turn increases the difference in momentum. So the higher momentum transfer per collision cancels the decreasing collision rate. The pressure independence of viscosity does not hold good at very low pressures when the mean free path becomes larger than the dimensions of the apparatus used or at very high pressures, which results in close interaction of the particles.

The tuning fork is made of a quartz crystal and hence exhibits piezoelectric effect, i.e. it acquires electric charges when it is subjected to mechanical stress and vice versa it oscillates when a voltage is applied to it, with a certain resonant frequency depending on the state of the medium in which it is contained.

As the viscosity of the gas containing the tuning fork increases due to an increase in temperature, damping affects the oscillatory motion of the tuning fork prongs thereby reducing its frequency. Therefore the resonant frequency of the tuning fork should increase with decreasing temperature. The reduced motion of the gas particles at lower temperatures results in less friction between particles, which diminishes the losses. Therefore the quality factor increases with decrease in temperature. A complication that arises when analysing the effect of temperature or pressure on the Q-factor is the difficulty in discriminating between the quality factor of the gas and the intrinsic quality factor due to the material of the fork. The intrinsic Q becomes

more dominant at lower temperatures. Generally the total quality factor Q_{TOTAL} can be related to the quality factor due to the gas Q_{GAS} and the intrinsic quality factor $Q_{INTRINSIC}$ due to the material of the tuning fork using:

$$\frac{1}{Q_{TOTAL}} = \frac{1}{Q_{GAS}} + \frac{1}{Q_{INTRINSIC}} \qquad (4.2.5)$$

4.2.3 Experimental Set-up

The Tuning Fork

We used commercially available tuning forks with a specified frequency of 32768 (2^{15}Hz) in vacuum made of a single α quartz crystal. The tuning forks are enclosed in a vacuum can and supported at the bottom by a ceramic base. Figure 4.2.1 shows the dimensions of the tuning fork inside the vacuum can.

By virtue of its piezoelectric property, the tuning fork can be driven by subjecting it to a mechanical force or exciting it electrically. We used the latter method. When a voltage is applied to the electrodes of the tuning fork, the tuning fork acts like an RLC series resonator whose equivalent circuit is shown in figure 4.2.2. [24].

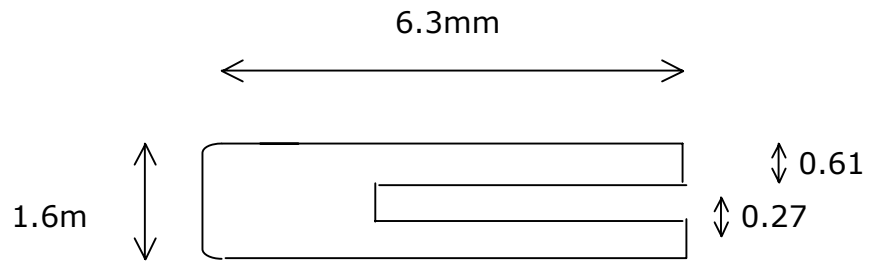

Figure 4.2.1: Dimensions of tuning fork

When the prongs of the tuning fork vibrate a current I_p is induced due to the piezoelectric effect of the quartz crystal. The capacitance of the tuning fork creates current I_0. The resonant frequency f_R and quality factor Q of the resonator are given by:

$$f_R = \frac{1}{2\pi\sqrt{L(C + C_0)}} \qquad (4.2.6)$$

$$Q = \sqrt{\frac{L}{[R(C + C_0)]^2}} \qquad (4.2.7)$$

The capacitance C_0 depends on the geometrical arrangement of the electrical leads of the crystal, its dielectric properties and the cable capacitances.

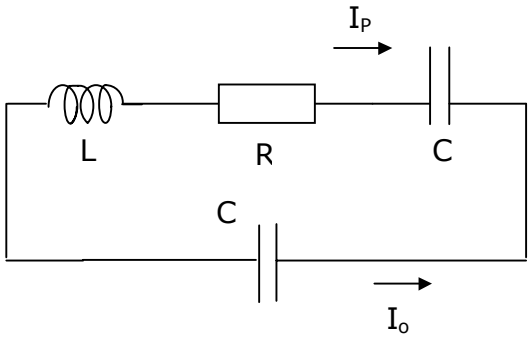

Figure 4.2.2: RLC equivalent circuit of tuning fork resonator.

Resonant Frequency and Quality Factor Measurement

Figure 4.2.3 shows the circuit diagram we used to measure the admittance of the tuning fork. The centre tap transformer provides two ac voltages. The lock-in amplifier measures the amplitude and phase of the output signal. The variable capacitor is used to balance the capacitance of the circuit, as the package capacitance of the tuning fork (denoted in figure 4.2.1 as C) would distort the shape of the resonance curve by introducing parallel resonances. C_v has to be varied such that the current through the

package capacitance of the tuning fork equals the current through C_v and these two currents cancel each other. We determined this value of C_v to be about 1.5pF.

To find the resonant frequency of the tuning fork we applied an ac voltage (0.1V) of sweeping frequency (in the range of 32500Hz to 33500Hz), using a function generator. The function generator and the lock-in amplifier are controlled by a Labview program, which sets the amplitude of the function generator and sweeps the frequencies in the range specified by the user. The output measured by the lock-in amplifier is fed back to the program and plotted against the frequency range to obtain the resonance curve.

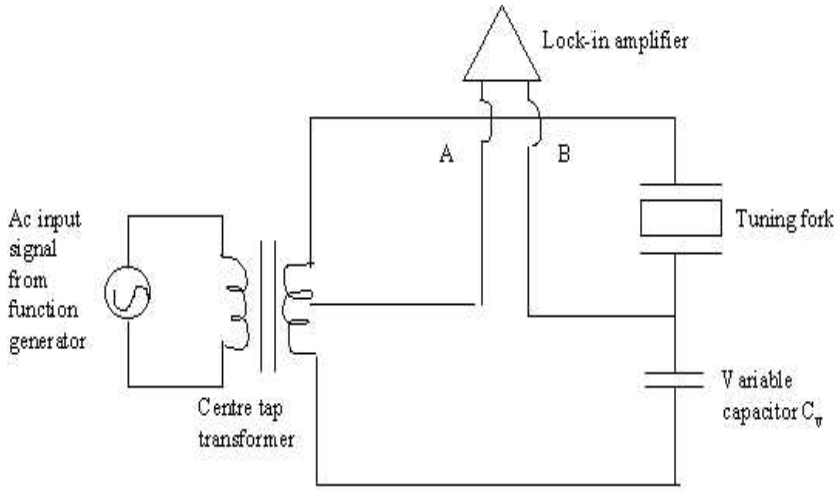

Figure 4.2.3: circuit diagram used to drive tuning fork and measure admittance

The program calculates the resonant frequency f_R, quality factor Q, resonance amplitude and phase. Figure 4.2.4 shows the graph of the resonance curve we measured at room temperature with the tuning fork in vacuum. The resonant frequency was about 32765Hz with a Q of 16924. The difference in the measured resonant frequency and the one given by the manufacturers as 32768Hz could be due to minor changes in the material of the crystal. To measure the parameters of the tuning fork as a function of temperature and pressure we first had to remove the tuning fork from its vacuum can. This can be done by crushing the ceramic base with pliers or by filing the top of the can off so that the tuning fork can be extracted carefully with its electrical contacts intact.

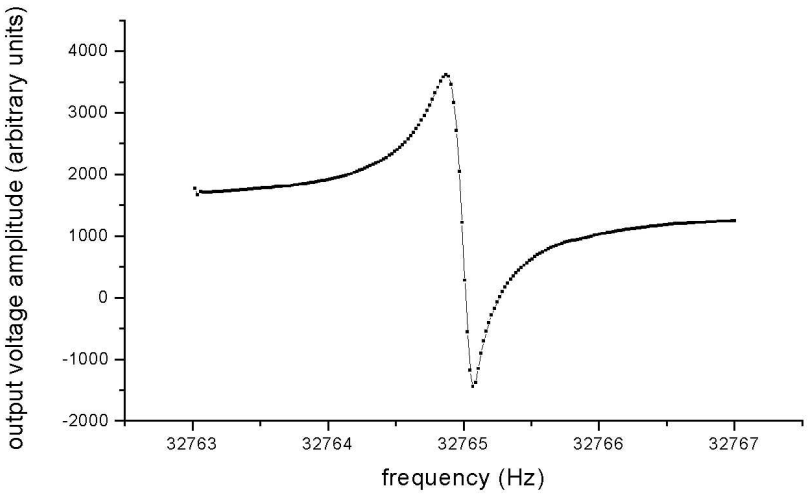

Figure 4.2.4: Resonance curve of the output voltage read by the lock-in amplifier as a function of frequency. The resonant frequency of the tuning fork was 32765Hz in vacuum.

The tuning fork was then inserted into a gas cylinder, which was filled up with air or helium gas. To create vacuum or vary the pressure a rotary vacuum pump was used.

Dependence of f_R and Q of tuning fork on pressure in air medium at room temperature
First the cylinder was filled with air and the resonance curve of the tuning fork at room temperatures was obtained by following the procedure given above at different pressures from about 0.08mbar to atmospheric pressure. The pressure readings were taken from a pressure gauge and the resonant frequency f_R and quality factor Q plotted against the pressure. These plots are shown in figure 4.2.5 and 4.2.6.

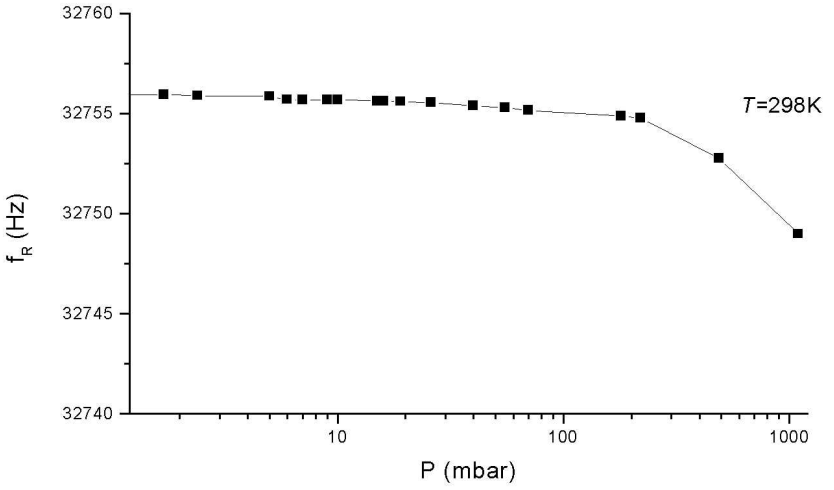

Figure 4.2.5: Graph of resonant frequency versus pressure at room temperature (289K) with the tuning fork in air inside the cylinder.

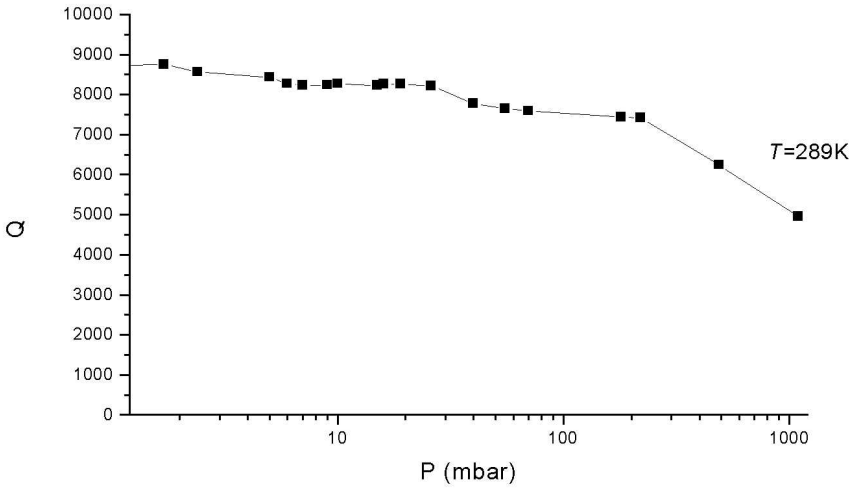

Figure 4.2.6: Graph of quality factor Q versus pressure at room temperature (289K) with the tuning fork in air inside the cylinder.

As predicted, both the resonant frequency and the quality factor have a lower value in air than in vacuum due to the presence of viscous damping exerted by air with f_R ranging from 32756Hz to 32748Hz and Q from 4955 to 7357. f_R does not vary much with the pressure in the region of about 0.1mbar to 200mbar, as the viscosity of a gas is independent of the pressure (see section 4.2.2). At pressures higher than 200mbar, f_R decreases with the pressure, which can be due to the pressure acting on the tuning fork, which has the effect of increasing its mass. Due to the added mass, the frequency at which the tuning fork prongs oscillate reduces. The drop in the Q indicates that the viscosity is not entirely independent of the pressure. This is pronounced, especially at higher pressures, which could be owing to the proximity of the gas molecules, which increases the rate of momentum-transfer collisions and therefore the viscosity, reducing in turn the quality factor.

Dependence of f_R and Q of tuning fork on pressure in Helium medium at room temperature and at 77K

Next the gas cylinder was filled with helium gas through the gas handling system and the resonant frequency and quality factor were measured at different pressures at room temperature (T=289K) as above. The gas cylinder containing the tuning fork was immersed in a can of liquid nitrogen (T=77K) and the experiment repeated. The graphs of f_R versus P at T=289K and T=77K are shown in figure 4.2.7 and 4.2.8 respectively. In figure 4.2.7 we can see that as expected the resonant frequency remains constant with increasing pressure till about 100mbar, at which point the resonant frequency drops due to the atoms being in close contact with each other as is the case when the tuning fork is exposed to air medium. Compared to the data measured from the air medium the resonant frequency is lower as Helium gas has a higher molecular mass than air and hence higher viscosity.

The graph showing the resonant frequency dependence on pressure at T=77K (figure 4.2.8) too shows that the resonant frequency is almost constant with increasing pressure. Again at the low end and the high end of the pressure range this pressure independence does not hold good due to mean path effect and proximity of atoms respectively. The calculation of the free mean path is given below.

The dependence of the Q factor on pressure is shown in figures 4.2.9 and 4.2.10. In both cases the quality factor is higher at low pressures, probably due to free mean path effects.

Calculation of Mean Free Path

The mean free path l is related to the viscosity η by

$$l = \frac{1}{\sqrt{2}n\sigma} \qquad (4.2.8)$$

where n is the number of atoms in the gas and σ the cross-sectional area of the atom. For helium gas at room temperature and 20mbar pressure we calculated the mean free path by first finding out the number of atoms n contained in the gas using $PV=nRT$, where P is the pressure, V the volume of the gas cylinder (V= 5*10^{-4}m^2, taking connecting tubes into consideration as well), R= 8.314Jmol^{-1}K^{-1} is the universal gas constant and T= 289K is the temperature. The number of atoms was calculated to be 9.41·10^{23}. Therefore the mean free path for ^{3}He gas in these conditions is 0.24mm, which is comparable with the dimensions of the tuning fork.

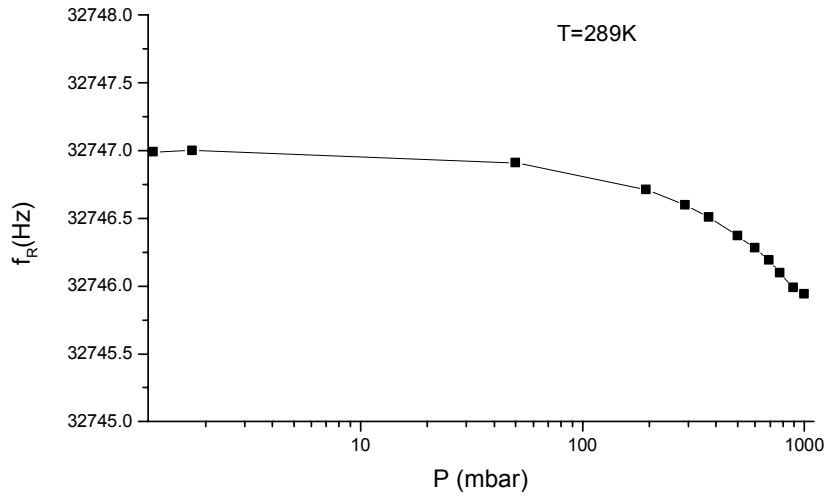

Figure 4.2.7: Graph of resonant frequency f_R (in Hz) versus pressure P (in mbar), when gas cylinder containing tuning fork is filled with ^{3}He gas at room temperature. (T=289K)

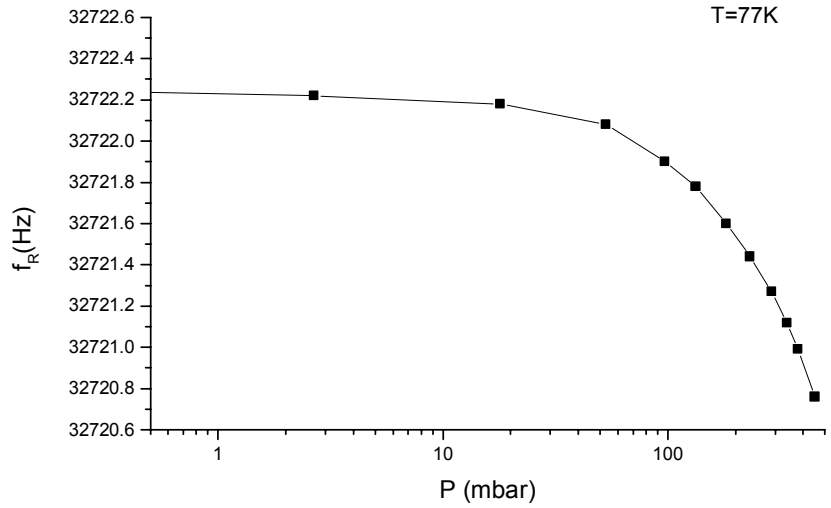

Figure 4.2.8: Graph of resonant frequency f_R (in Hz) versus pressure P (in mbar) when gas cylinder containing tuning fork is filled with ^{3}He gas and immersed in liquid nitrogen. (T=77K).

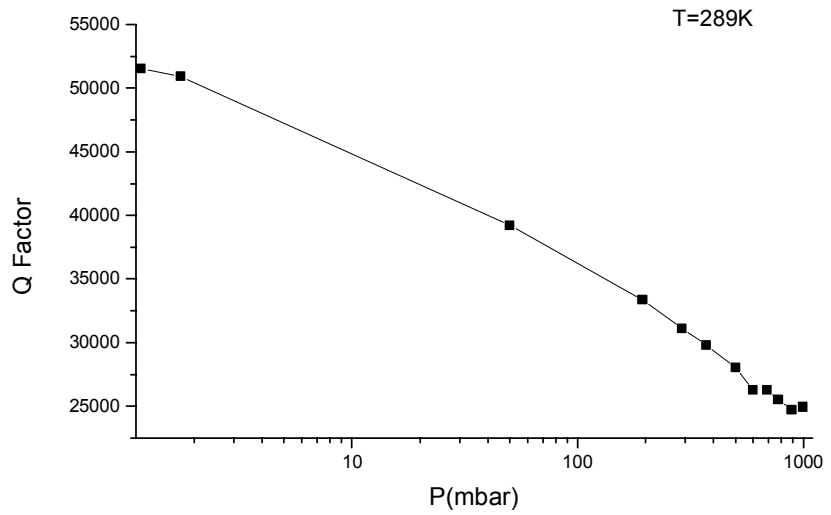

Figure 4.2.9: Graph of quality factor Q versus pressure P (in mbar), when gas cylinder containing tuning fork is filled with ^{3}He gas at room temperature. (T=289K)

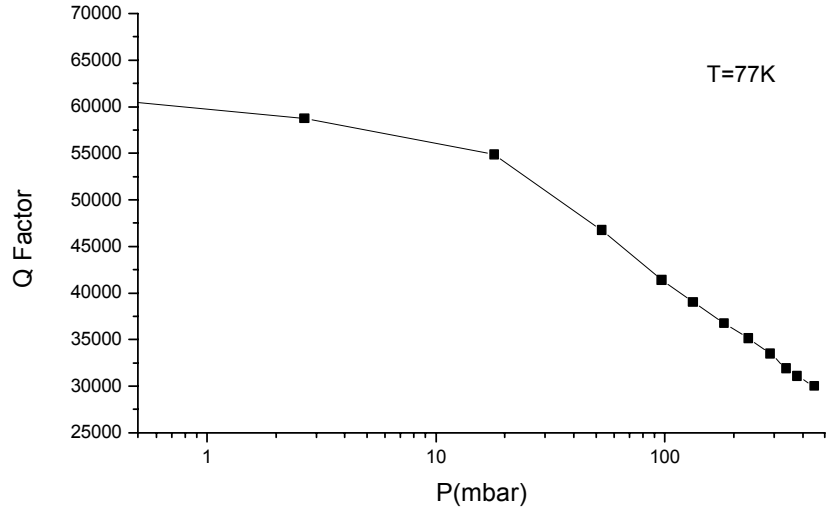

Figure 4.2.10: Graph shows Q as a function of pressure *P* when tuning fork is contained in Helium gas when gas cylinder is immersed in liquid nitrogen can (*T*=77K).

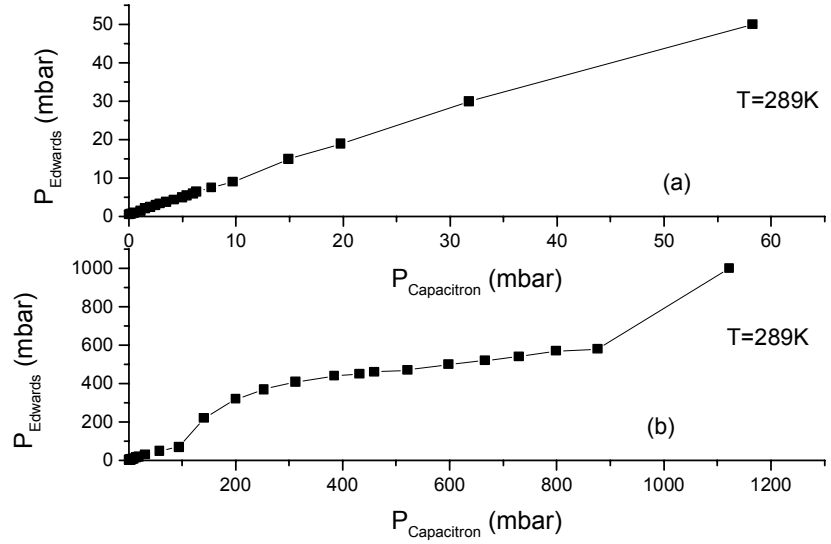

Figure 4.2.11: Graph shows comparison of Capacitron and Edwards pressure gauge at room temperature. Figure (a) shows linearity of Edwards pressure gauge up to 58mbar. Figure (b) shows comparison between pressure gauges between 0.55mbar to 1100mbar.

Pressure Calibration

The pressure was measured using two gauges, a Capacitron pressure gauge and an Edward Pirani pressure gauge. The working of the Capacitron pressure gauge is based on the change in the capacitance of the material with pressure and is sensitive at pressures above 1mbar. A Pirani pressure gauge uses the principle of heat conduction and proved to be more sensitive at temperatures below 50mbar. Figure 4.2.11 shows a comparison of the two pressure gauges, when the pressure is varied in the vacuum chamber containing air. The plot shows that the Edwards pressure gauge readings are linear below 50mbar. Thus, the Edwards pressure gauge was used to measure the pressures below 50mbar and the Capacitron pressure above that.

Dependence of Resonant frequency and Quality Factor on Temperature in Helium mixture of Dilution Refrigerator

The same tuning fork was then mounted on the sample plate above the sample cell in the dilution refrigerator and the resonant frequency and the quality factor were measured at decreasing temperatures starting from 1.8K down to 18mK. The applied magnetic field was 14.86T. As reference the temperature displayed by the mixing chamber refrigerator thermometer was used.

The resonant frequency and quality factor measured were plotted against the temperature as shown in figures 4.2.12 and 4.2.13. The resonant frequency decreases by about 700Hz as compared to when the tuning fork is in gas medium. The resonant frequency in the Helium mixture fluctuates a lot between 250mK and 18mK after which it constantly reduces with increasing temperature. This unusual temperature dependence is thought to be due to the slipping movement of the tuning fork at the surface of the Helium mixture.

The quality factor is lower in the Helium liquid than in the gas due to the friction, resulting in increased losses, exerted by the liquid. Figure 4.2.14 shows the Q data measured by Clubb [22] when the tuning fork was inserted in ^{3}He-^{4}He mixture and pure ^{3}He. The Q-factor is higher when the tuning fork is contained in the mixture rather than in pure ^{3}He owing to the increased viscosity of pure ^{3}He. In our case, when the tuning

fork is inside the mixing chamber, there is no definite way of knowing if the tuning fork is contained in the helium mixture or pure ^{3}He as we cannot estimate where the phase boundary will be formed. Comparing Clubb's data to the Q values we measured (figure 4.2.14) proves that the tuning fork most likely is in the Helium mixture.

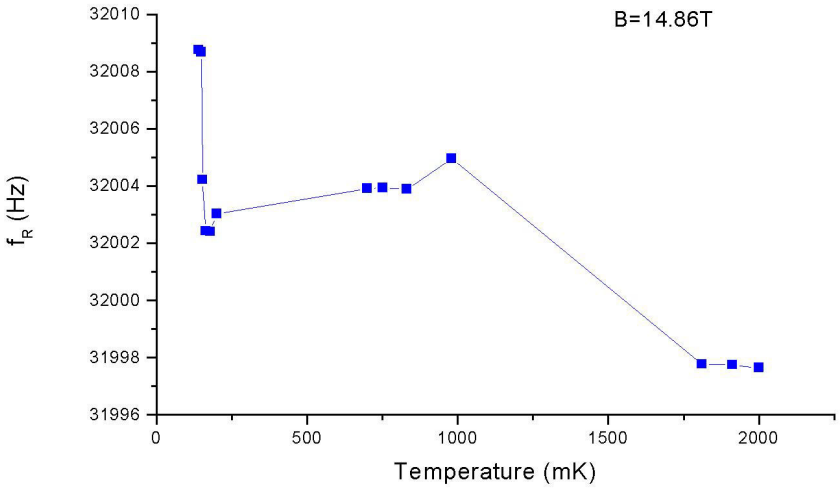

Figure 4.2.12: Graph of resonant frequency f_R (in Hz) versus temperature T, when the tuning fork was mounted above the xenon sample inside the mixing chamber of the dilution refrigerator. The applied field was 14.86T.

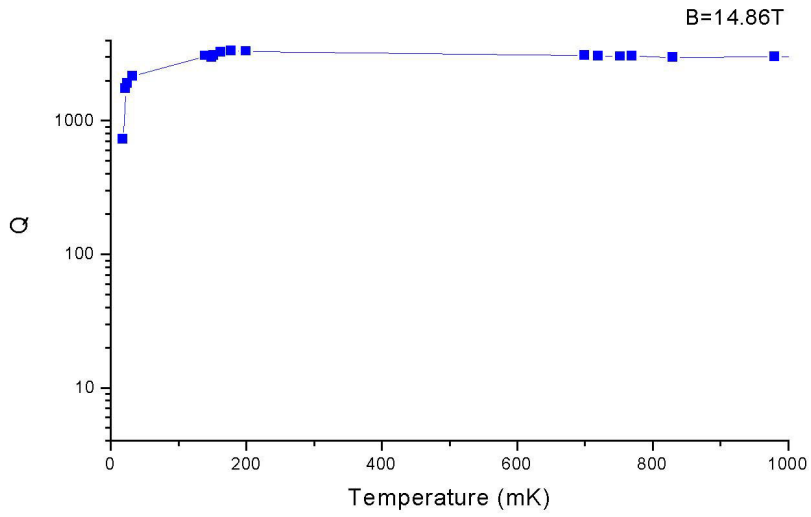

Figure 4.2.13: Graph of quality factor Q versus Temperature T, when the tuning fork was mounted above the xenon sample inside the mixing chamber of the dilution refrigerator. The applied field was 14.86T.

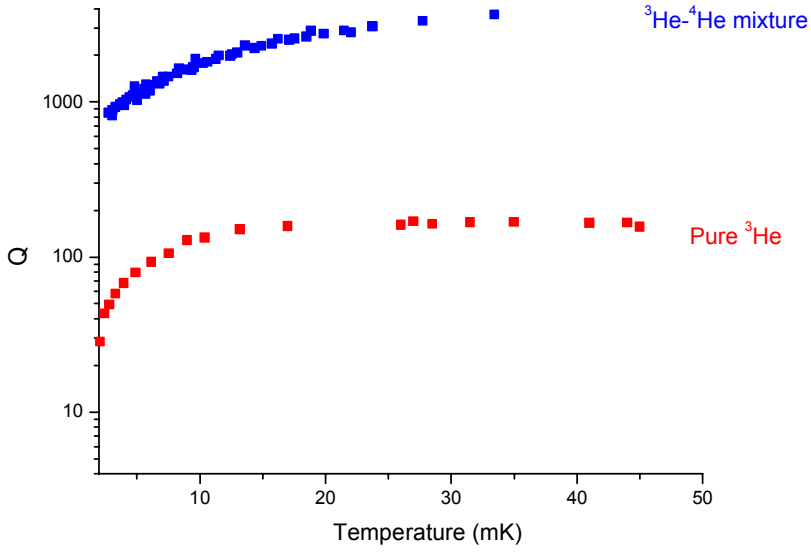

Figure 4.2.14: Graph showing quality factor Q as a function of temperature T in both pure ^{3}He and a mixture of ^{3}He-^{4}He [22]

Calibration

According to the data obtained by Clubb [22], the Q-factor shows a linear $T^{2/3}$ dependence. This dependence can be used for viscosity-temperature calibration purposes. The viscosity of a fermi liquid at low temperatures varies as $\eta \propto \frac{1}{T^2}$. Therefore the viscosity and the quality factor can be related to each other using:

$$\frac{1}{Q} \propto T^{-2/3} \qquad \text{or} \qquad Q^3 \propto \frac{1}{\eta}$$

Zeegers et al [27], who investigated the use of vibrating wires in a saturated ^{3}He-^{4}He mixture below 200mK, have found an empirical formula to relate viscosity and temperature for temperatures below 80mK:

$\eta T^2 = a + bT$

where a=$2.7 \pm 0.2 \cdot 10^{-8}$ PasK^2 and b=$34 \pm 3 \cdot 10^{-8}$ PasK.

4.2.4 Conclusion

The data from the experiments performed on tuning forks at different pressures and temperatures and in different media by and large conform to the expected theoretical behaviour and are also consistent with the results from the literature. The calibration equations need to be carefully fitted. As this method of thermometry is mostly field independent and the set-up is very easy and inexpensive it is very likely to be used more often in low-temperature high-field thermometry applications.

4.3 RESISTANCE THERMOMETRY

4.3.1 Introduction

We are using three resistance thermometers; two thick film chip Ruthenium Oxide (RuO_2) resistors (RuO_2 –I and RuO_2 –II) and one Cernox (Ceramic Oxynitride) resistor, all of which are mounted around the sample space inside the dilution refrigerator. Resistance thermometers have been widely used in low temperature thermometry mainly due to their ready availability and the ease of measurement [15]. They are usually accurate over a wide temperature range and facilitate digital and analog control and display. A commonly used resistance thermometer is made of Platinum, which is popular because of its chemical inertness and its ductility. Its drawback is that the linear temperature dependence of its resistance deteriorates below 50K. At low temperatures Germanium resistance thermometers are often used as they give accurate temperature measurement results even below 40K but they exhibit strong magnetic field dependence [28], unlike RuO_2 resistance thermometers, which have a magnetoresistance of less than 1% for temperatures below 1K and fields up to 8T. The Cernox (Ceramic Oxynitride) thermometers (which are provided by Oxford Instruments [16] along with the dilution refrigerator just as the RuO_2 thermometers) too have high magnetoresistance below 2K. The temperature range specified by Oxford Instruments for RuO_2 thermometers, ranges from 25mK to 4.2K depending on the excitation current applied [28]. RuO_2 thermometers are also advantageous because of their relatively small size, low weight (of a few milligram), low cost and the reproducibility of their behaviour after thermal cycling. We took temperature readings using two RuO_2 thermometers mounted on opposite sides of the sample space and the Cernox thermometer from 1.8K down to 18mK. The Cernox thermometer measured the temperature down to about 1.4K and the RuO_2 thermometer as low as 18mk

4.3.2 Physical Background

Resistance thermometers are based on the temperature dependence of resistance of conductors, semiconductors or carbon resistors. The vibration of the atoms of the conductor and the probability of collisions among atoms are proportional to the temperature. As these factors affect the conductivity of the material, the resistance of changes with thermal excitation. According to the temperature coefficient (change of resistance with temperature) the resistance increases with temperature (positive temperature coefficient) or decreases with temperature (negative temperature coefficient). If there is a finite increase of temperature, R is the resistance at temperature T and R_0 is the resistance at a reference temperature T_0, then the variation of resistance with temperature can be described by a third order polynomial [29]:

$$R=R_0[1+A\Delta T+B\Delta T^2+C\Delta T^3] \qquad (4.3.1)$$

Where $\Delta T=T-T_0$ and the coefficients A and B are independent of temperature and given by [29]:

$$A=\frac{1}{R_0}\left[\frac{\partial R}{\partial T}\right]_{T=T_0}$$

$$B=\frac{1}{2!R_0}\left[\frac{\partial^2 R}{\partial^2 T}\right]_{T=T_0}$$

$$C=\frac{1}{3!R_0}\left[\frac{\partial^3 R}{\partial^3 T}\right]_{T=T_0} \qquad (4.3.2)$$

To obtain a linear temperature dependence we can approximate equation *(4.3.1)* when T_0=273K as:

$$R_0=[1+\alpha T] \qquad (4.3.3)$$

Where $\alpha = \frac{1}{R_0}\frac{R_{373} - R_0}{373}$ is the coefficient of temperature, normally taken as an average value over a given temperature range. According to the temperature coefficient the resistance increases with temperature (positive temperature coefficient) or decreases with temperature (negative temperature coefficient). As there is no single and simple temperature dependence, resistance thermometers are usually used as secondary thermometers.

4.3.3 Temperature Measurement using RuO_2 and Cernox Thermometers

The RuO_2 and Cernox thermometers are fixed to the sample plate inside the mixing chamber of the dilution refrigerator. The magnetic field applied when these measurements were taken was about 15T. The sensor of the RuO_2 is mounted by the manufacturers in a gold-plated copper holder, which provides mechanical protection for the sensor. The RuO_2 and Cernox thermometers are connected to a temperature controller through an ac resistance bridge, which provides the required excitation current for temperature measurement. Depending on the temperature range required, the ac excitation current should be as small as possible. The temperature controller allows the resistance of the thermometers to be read directly from the digital display.

To test the thermometers we took readings of the resistance thermometers, tuning fork parameters and the temperature of the mixing chamber while cooling down the sample using the dilution refrigerator from a temperature of 1.8K down to 18mK. The Cernox thermometer could not read temperatures below about 1.4K. Both the Cernox and the RuO_2 thermometers exhibit a negative coefficient of temperature, i.e. their resistance decreases with increase in temperature. To convert the resistance reading from the temperature controller into temperature the data is plotted according to *ln (1/T)* versus *ln (R-R_o),* where *R* is the resistance at temperature *T* in Kelvin and R_o is the resistance at room temperature taken as 2.21kΩ [16].

For fitting the data we used a third order polynomial described by the equation:

$$ln(1/T)=\sum_{i=0}^{3} a_i [ln(R- R_o)]^i \qquad (4.3.4)$$

The best fit was provided by Oxford Instruments from empirical data as:
$a_0 = -0.6878755$, $a_1 = 1.1039783$, $a_2 = 0.0556154$ and $a_3 = -0.0103092$. We used this equation to write a Labview program that converts the resistance into temperature.

The plot of the data fitted using equation *(4.3.4)* of the calculated temperature against the resistance measured (figure 4.3.1) for
RuO_2-I shows an exponential decay. This graph can be used as reference for future resistance to temperature conversions. Next we plotted $ln(1/T)$ against $ln(R-R_o)$ (figure 4.2.2), which shows the linearity for this fit in the measured temperature range. Figure 4.3.3 indicates that there is a slight difference in the resistance measurements of RuO_2 -I and RuO_2 -II, which could be due to very minute differences in their resistivity brought about during the manufacturing process.

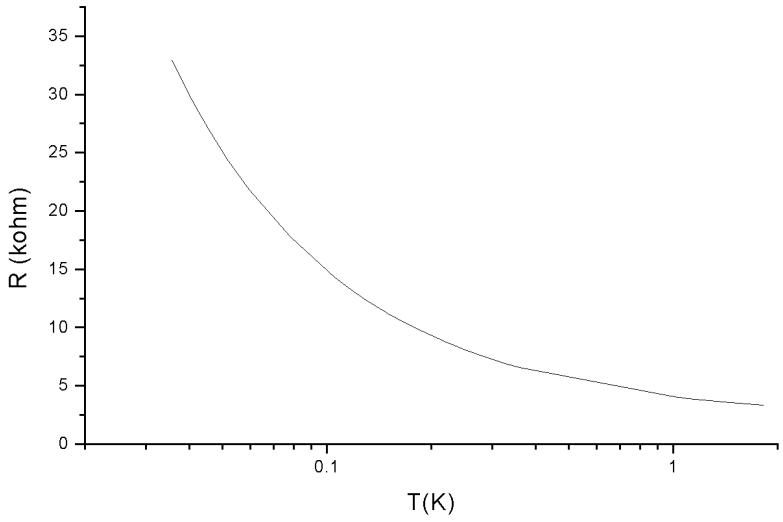

Figure 4.3.1: The figure shows the exponential dependence of the Resistance R measured by the RuO_2 -I resistor on temperature T.

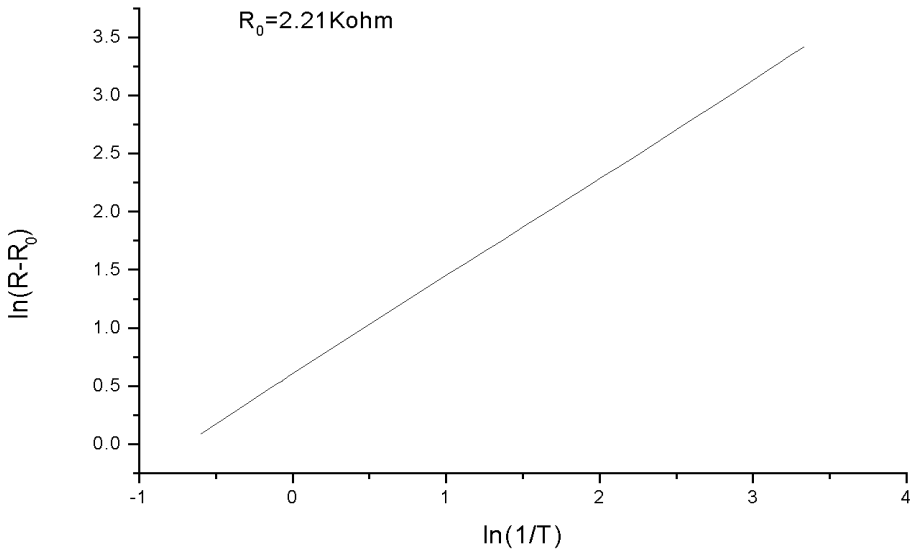

Figure 4.3.2: This figure shows the logarithmic dependence of the resistance R on the temperature 1/T with respect to the reference temperature $R_{0,}$ which is taken as 2.21k using the fit specified by Oxford Instruments.

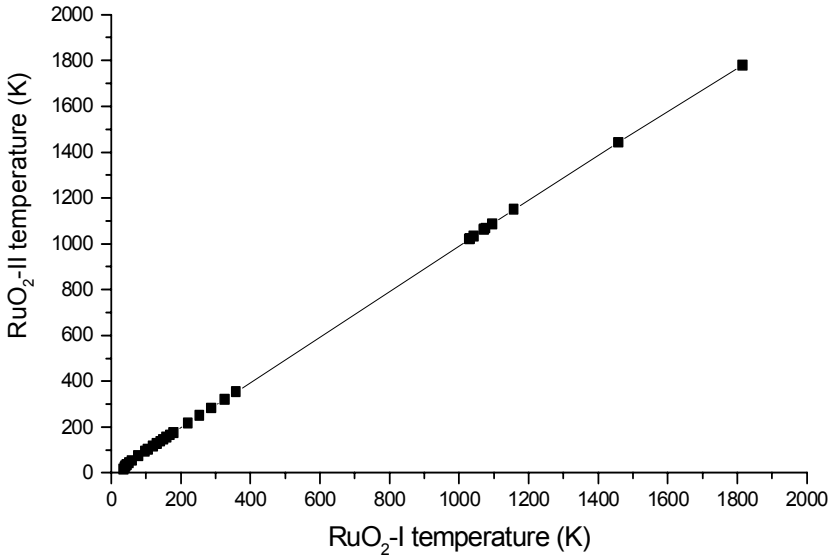

Figure 4.3.3: Comparison of the temperature readings obtained from the resistances measured by the two RuO_2 thermometers. The slight non-linearity could be due to differences in their materials resulting in different resistivities.

4.4 COULOMB BLOCKADE THERMOMETER

4.4.1 Introduction

The Coulomb Blockade Thermometer (CBT) is based on the conductance drop across tunnel junctions. Pekola et al [30] have shown that tunnel junction arrays between metal electrodes can be used for primary thermometry, and have studied the dependence of the V-I characteristic (and therefore of the differential resistance and conductance) on temperature. The commercially available Nanoway CBT primary thermometer [21] provides simple primary and secondary thermometry over a temperature range (from 20mK to 1K) using small on-chip sensors. Its magnetic field independence makes it particularly suitable for our project. To test the required working and circuit conditions of this device, we constructed the required electrical circuit and tested its working using a diode and a resistor in place of the CBT. The V-I characteristic measured at room temperature agrees with the expected graph provided by Nanoway from their experiments with the CBT at temperatures below 1K. The CBT has yet to be tested at lower temperatures, after which it will be inserted into the cryostat and used for primary and secondary thermometry.

4.4.2 Physical Background

The operation of the CBT is based on the principle of the Coulomb blockade [31]. The Coulomb blockade causes an increase in resistance of a tunnel junction when the bias voltage applied is too low to allow tunnelling of electrons through the junction. To understand the formation of a Coulomb blockade we can consider the junction to be made of a capacitor, which consists of an insulating material between two metal electrodes. The energy required for one electron to tunnel through the junction is given by the charging energy or coulomb energy $E_c = e^2 / 2C_\Sigma$, where C_Σ is the total capacitance of the junction and e is the charge of the electron. Therefore if a voltage less than $V=e/C_\Sigma$ is applied across the junction, the energy of the capacitor will be insufficient for electrons to pass through it. The phenomenon of a reduced tunnelling

current flowing through the junction when its voltage is below $V=e/C_\Sigma$ is called Coulomb blockade. If the charging energy E_c is much smaller than the thermal energy k_BT, where k_B is the Boltzmann constant and T the temperature, then thermal excitation allows electrons to pass through the Coulomb blockade. This temperature dependence of the behaviour of a Coulomb blockade allows it to be used for thermometry.

From the above discussion it can be seen that at temperature T the thermal energy k_BT, the electric potential voltage eV and the charging energy E_c determine the conductance of a tunnel junction. If N is the number of junctions in series, G the conductance, R_T the resistance at temperature T and $G_T = (2R_T)^{-1}$ the asymptotic conductance, then the dynamic conductance was derived by Pekola et al as:

$$G/G_T = 1-(E_c / k_B\ T)\ g(eV/N\ k_B\ T) \qquad (4.4.1)$$

Where the function g is given by:

$$g(x)=[x\sinh(x)-4\sinh^2(x/2)] / [8\sinh^4(x/2)]. \qquad (4.4.2)$$

Pekola et al have shown that if all junction arrays considered have the same number of junctions in series then $V_{1/2}$, the full width at half maximum divided by the temperature is a constant.

From equation *(4.4.1)* we can see that $V_{1/2}$ is proportional to T. If the number of junctions N is known and if all junction arrays of the CBT have the same number of junctions then the ratio of $V_{1/2}$ and T is constant. Therefore $V_{1/2}$, i.e. the full width at half maximum of the conductance curve, given by G/G_T versus the applied bias voltage provides the primary thermometer quantity, which is specified by Nanoway as

$$V_{1/2} = 5.439N\ k_B\ T/e$$

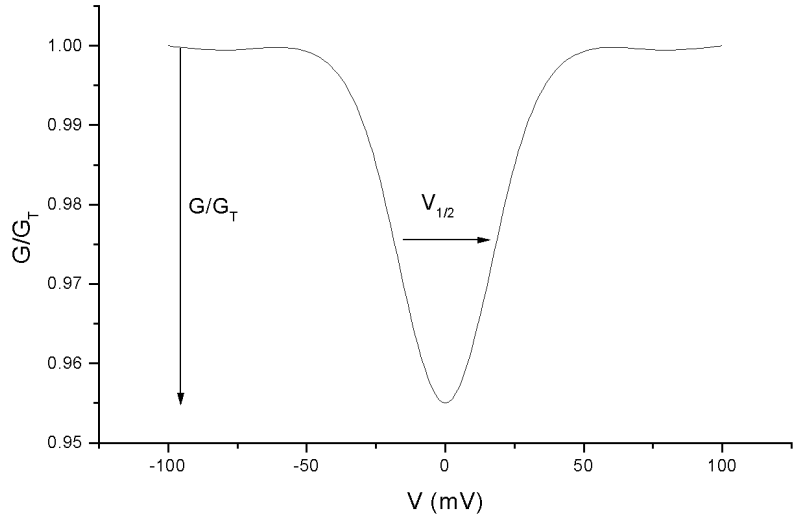

Figure 4.4.1: The graph shows the dynamic conductance G/G_T as a function of the bias voltage V_{bias}. $V_{1/2}$ is the full width at half maximum and G/G_T is the depth of the conductance curve.

We can also see that the dynamic conductance varying with the bias voltage applied is inversely proportional to the temperature. From equation (4.4.1), one can derive the expression

$$\Delta G/G_T = E_c / 6k_BT$$

The dynamic conductance is inversely proportional to the temperature and the depth of the conductance curve can be used for secondary thermometry. Figure 4.4.1 shows the conductance curve of G/G_T as a function of the bias voltage V_{bias}. The temperature T can be calculated under the condition that $E_c / k_B \ T \rightarrow 0$. As the conductance drop is in practise not zero, a linear correction, which has been calculated analytically in [32] has to be applied to $V_{1/2}$ which is given by the manufacturers of the Nanoway CBT as $V_{1/2} / V_{1/2,0} = 0.39211 \ \Delta G/G_T$, where $V_{1/2,0}$ is the full width at half minimum of the conductance drop.

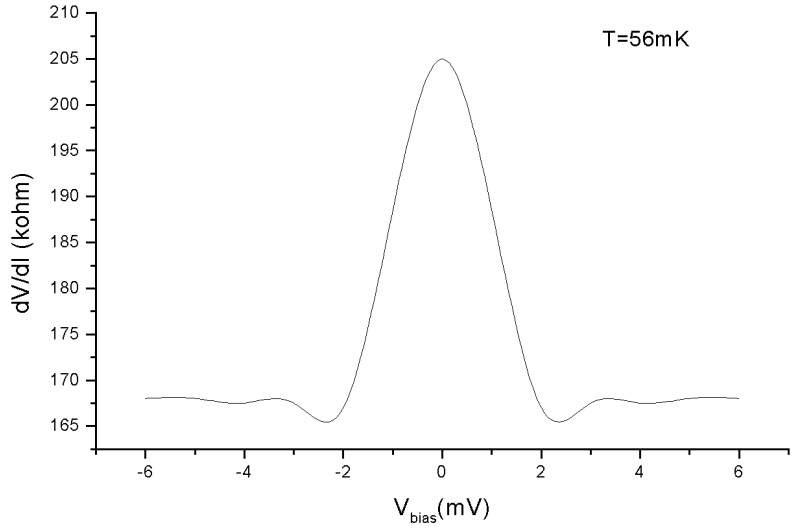

Figure 4.4.2 a): Plot of differential resistance dV/dI versus bias voltage V_{bias} at 56mK. [21]

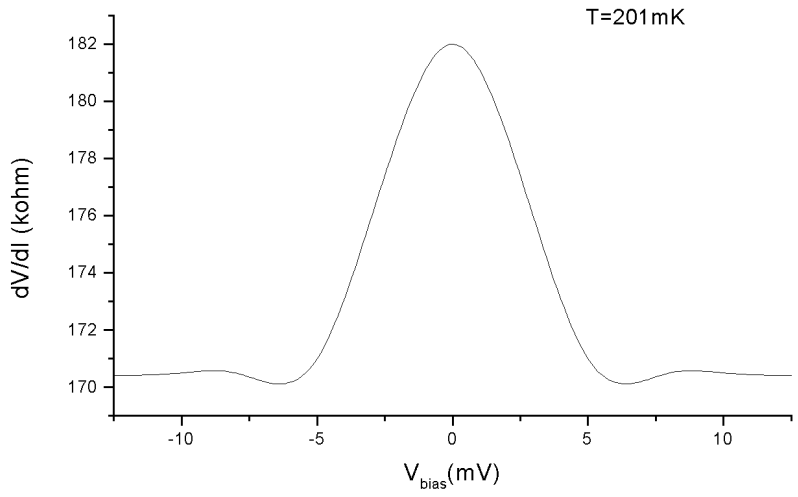

Figure 4.4.2 b): Plot of differential resistance dV/dI versus bias voltage V_{bias} at 201mK. [21]

Figures 4.4.2 a) and b) show the plot of the differential resistance *dV/dI* with the applied bias voltage V_{bias} at 201mK and 56mK respectively. Note the reduced width of the curve at the lower temperature.

The Nanoway CBT primary thermometer was tested by the manufacturers in magnetic fields up to 31 T and a temperature range from 0.4K to 4.2K. The test data

[21] show that the temperature reading of the CBT is not affected by the magnetic field in this range.

For the application scope of the CBT a few limitations have to be taken into consideration. The CBT has a wide temperature range but it is limited at high temperatures by the signal to noise ratio and by the Coulomb blockade at low temperatures. At low temperatures one may encounter problems caused by charge sensitivity. Also the sensor contains aluminium, which superconducts below 1.4K. Therefore at these temperatures a magnetic field applied perpendicular to the plane of the sensor chip of about 0.1 to 0.2 T is required to keep the sensor in the normal state. Pekola et al [30] have found that variations of $V_{1/2}$ up to 5% can occur at 4.2 K. Care should be taken to keep the bias voltage stable.

4.4.3 Construction

The sensing element of the Nanoway CBT sensor 0.1, shown in figure 4.4.3, has four parallel arrays [21]. Each array consists of 40 junctions connected in series. The sensors are fabricated on a Silicon substrate by electron beam lithography. Using ultrasound bonding the arrays are linked to phosphor bronze wires of 0.15mm diameter. An overlying teflon piece and Stycast 2850 FT epoxy serves as mechanical protection. The CBT is about 3mm long, 1.5 mm high and 2 mm wide. The resistance of the CBT sensor is 184 kΩ at 300K and 210 kΩ at 4.2 K.

4.4.4 Experimental Set-up

To read the temperature in the primary mode the differential resistance *dV/dI* has to be measured as a function of the bias voltage V_{bias}. In the secondary thermometry mode no bias is applied. A uniformly increasing dc voltage is applied to the circuit shown in figure 4.4.4, which incorporates the CBT, in addition to the driving ac voltage V_{ac}. The ratio of the ac voltage drop across the device to the excitation current is measured. This gives the differential resistance *dV/dI*.

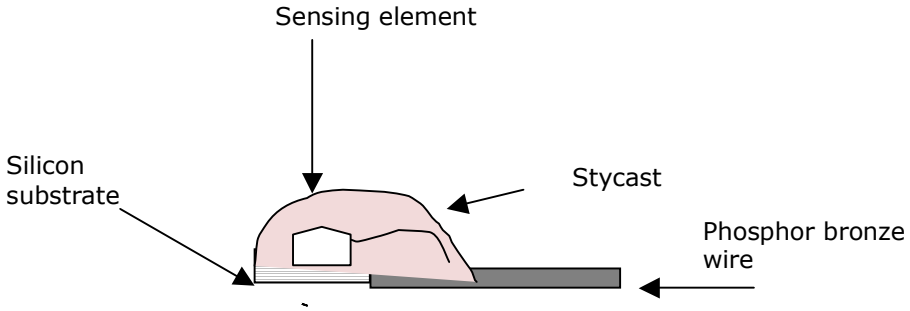

Figure 4.4.3: Construction of Nanoway CBT sensor 0.1 [21]

To test the electrical circuit we first connected a diode in place of the CBT. As the pn junction diode allows tunnelling of electrons when its depletion width is sufficiently small or an adequately large voltage is applied it can be used to study the working conditions of the CBT. A Labview program was written, which allows the dc bias voltage V_{bias} to be swept (using the DAC output of a lock-in amplifier, which was more stable with respect to time compared to the dc voltage provided by the function generator) across the specified range and sets the ac voltage V_{ac} of the function generator. The 1.7 MΩ resistor reduces the input signal to protect the device from large voltages. The voltage across the diode was measured using the lock-in amplifier whose output was fed back into the program, which then plotted the V_{bias} - V_{ac} characteristic. Figure 4.4.5 shows this plot of the expected decline in the output ac voltage V_{ac} with increasing V_{bias} displaying clearly that at about V_{bias} =0.7V, the turn-on voltage for a silicon diode, the diode becomes forward biased and starts conducting which reduces the output voltage $V_{ac.}$ We then connected a fixed resistor of 180 kΩ, which corresponds to the resistance of the CBT and ran the experiment again. The voltage across the 180kΩ resistor remains the same when V_{bias} is swept and therefore we obtained a constant output from the lock-in amplifier. To calculate the differential resistance *dV/dI* we connected again the diode.

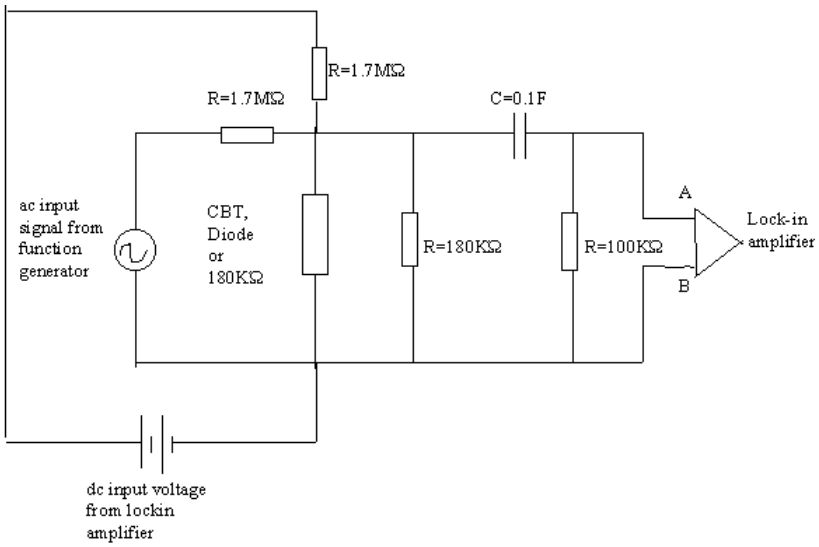

Figure 4.4.4: Circuit diagram, which incorporates the diode, 180kΩ resistor or the CBT.

As the variation of *dI* for this set-up and the purpose of testing the circuit was negligible, *dI* was assumed to be constant. We calculated the current *dI* using Kirchhoff's laws in the Labview program and plotted the differential resistance against the bias voltage. Figure 4.4.6 shows the graph of *dV/dI* versus $V_{bias.}$ The data we obtained agrees with the data provided by Nanoway shown in figure 4.4.2 a) and b) as the full width at half maximum of the differential resistance is wider at room temperature and would narrow down as the temperature decreases. The flat tip of the curve may be due to saturation of the lock-amplifier.

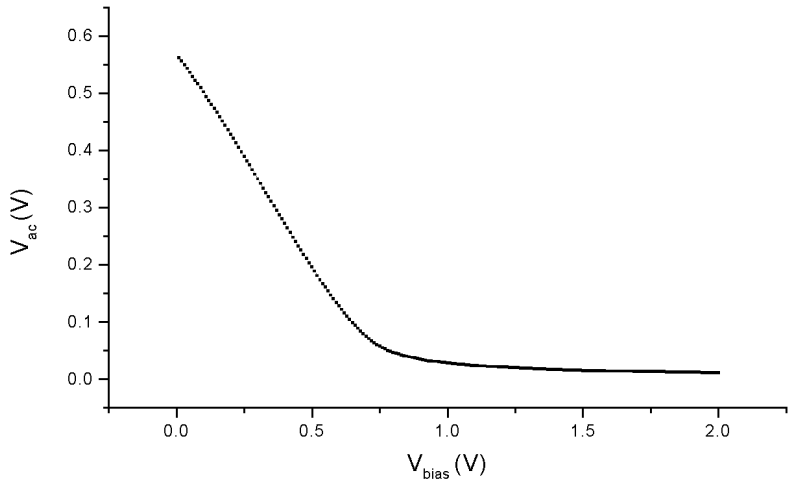

Figure 4.4.5: Graph showing the ac output voltage V_{ac} as a function of the dc bias voltage V_{bias} when the diode is connected in the circuit.

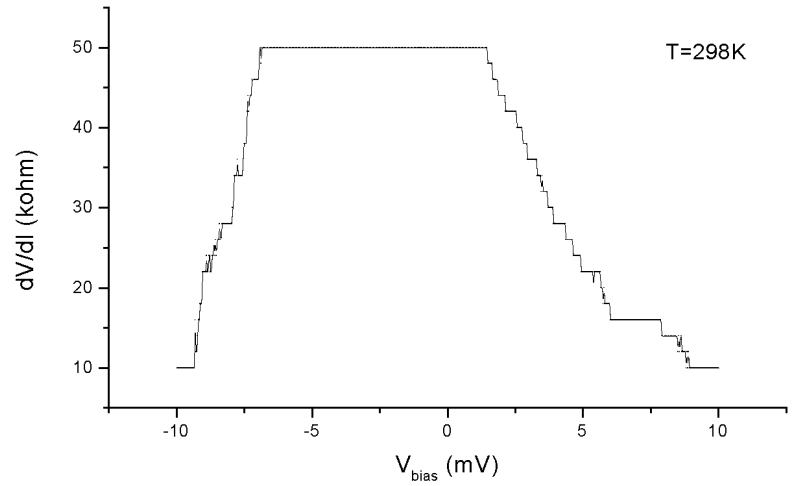

Figure 4.4.6: Plot of dc bias voltage V_{bias} versus the differential resistance dV/dI calculated by the Labview program with the diode connected in place of CBT.

4.4.5 Conclusion

We constructed the electronics for the CBT and tested the circuit at room temperature. Owing to its high sensitivity and magnetic field independence the CBT is a suitable device for our project. It will be tested at various lower temperatures in the near future and then mounted in the cryostat and used for measuring temperatures in a slightly higher temperature range than the tuning fork or the resistance thermometers.

CHAPTER 5

THE SPECTROMETER

In order to monitor the polarisation of the ^{129}Xe sample, pulsed NMR was employed. An RF pulse must be transmitted into the sample and the NMR signal generated in the coil by the nuclear magnetisation has to be detected and sent to a computer for display. These functions are performed by the NMR spectrometer. In this chapter, the NMR spectrometer and the coupling circuits used to transmit RF pulses to the ^{129}Xe sample inside the probe and receive the signal from the sample are described along with the problems that were encountered in their set-up. The spectrometer was designed by the workshop. The coupling circuitry and the required software programs to control the spectrometer were designed, constructed and tested by the project group. The spectrometer consists basically of a transmitter and a receiver. The transmitter generates RF pulses, according to the pulse parameters set by the triggering software (Labview), at the required frequency, which are then passed through the coupling circuitry to the sample in the probe. Similarly the FID signal from the sample passes through the coupling circuits to the receiver, which is interfaced again with a computer, which displays the FID in graphical form. The desired pulse sequences and specific parameter values are generated by the computer according to the parameter values specified by the user and communicated to the spectrometer through a data acquisition card.

The block diagram (figure 5.1) shows the different components of the whole spectrometer and how they are connected to each other. The design and working of the spectrometer, coupling circuits and the Labview program are briefly explained in the following sections. The front panel of the Labview program that generates the pulse sequences is shown in figure 5.6.

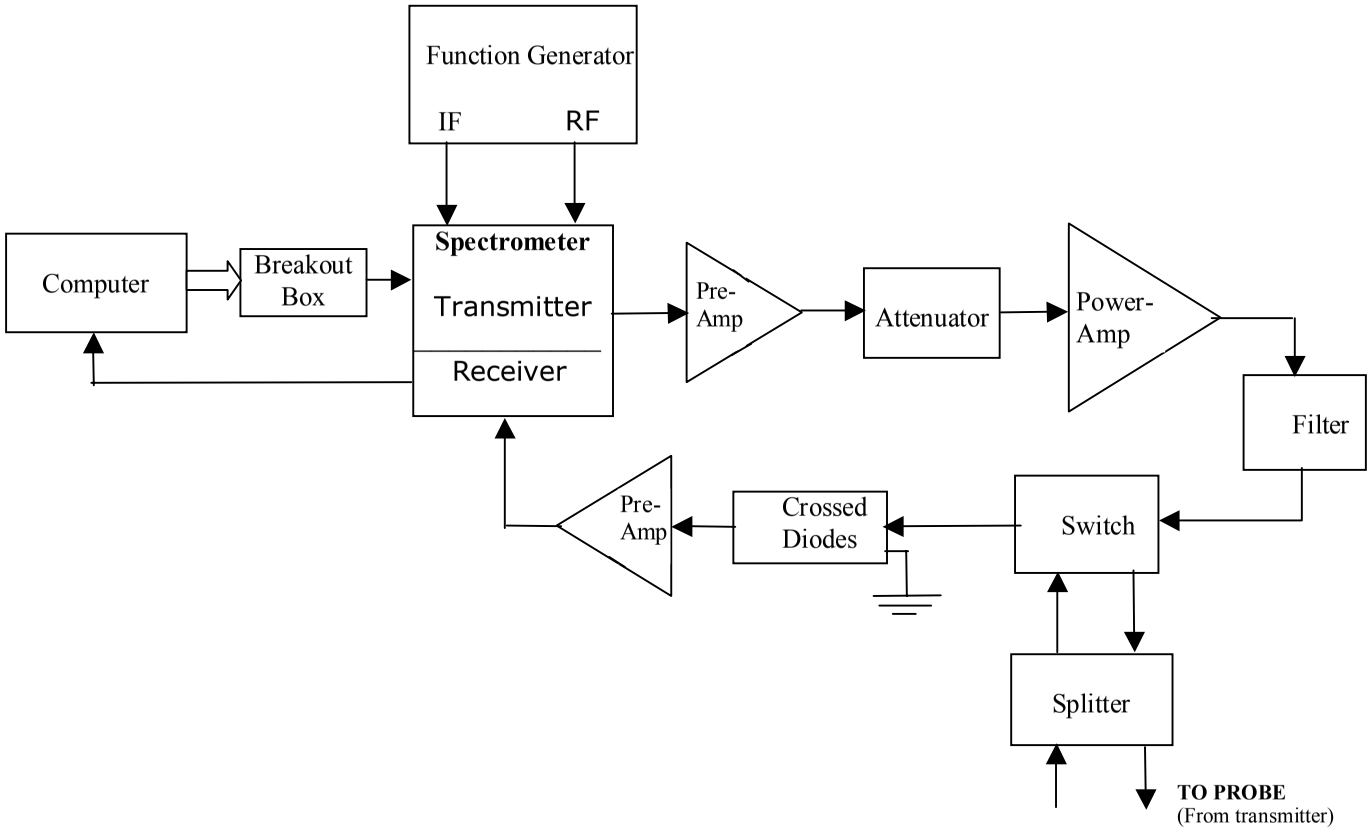
Function Generator
IF
RF
Computer
Breakout Box
Spectrometer
Transmitter
Receiver
Pre-Amp
Attenuator
Power-Amp
Filter
Switch
Crossed Diodes
Pre-Amp
Splitter
TO PROBE
(From transmitter)

During the experiments, the spectrometer described below proved to be inadequate, due to low signal to noise ratio and insufficient gain in the receiver and the transmitter. Thus, we used a different spectrometer, with a better signal to noise ratio and gain, whose working principle and construction are the same except that the transmitter and receiver are physically separate from each other. Improvements are being made to the original spectrometer.

5.1 The Spectrometer

The spectrometer incorporates both the transmitter and the receiver in one instrument. Figure 5.2 shows a schematic diagram of the spectrometer. It is heterodyne and uses an intermediate frequency (IF), in this case 10MHz, which is provided by the function generator (Stanford Research Systems, Model-D5335). It is divided by divider D1 into two signals, one of which drives the quadrature IF gates of the spectrometer and the other one goes to the quadrature detector in the receiver.

The transmitter IF is then passed through a stage of three dividers D1, D2, D3 and D4, which creates four signals of 0°, 90°, 180° and 270° phase shift. These four signals then pass through two mixers each (Mixer1-Mixer8). A 5V software trigger turns on the gate for the signal with the selected phase, which is taken through the 4-way combiner to the single side (SSB) band generator. The signal is amplified and split into two out of phase components in D5, which are both taken to the mixers Mixer 10 and Mixer 11 where they are mixed with the 150MHz RF local oscillator signal coming from the function generator. If the spectrometer is to be used with another Larmor frequency D6 can be unplugged and replaced.

The frequency of the IF signal f_{IF} and that of the local oscillator f_{LO} are mixed, resulting in and RF output giving the Larmor frequency f_0. For example if f_{IF}=186MHz and f_{LO}=10MHz, then f_{IF}* f_{LO}=176MHz.

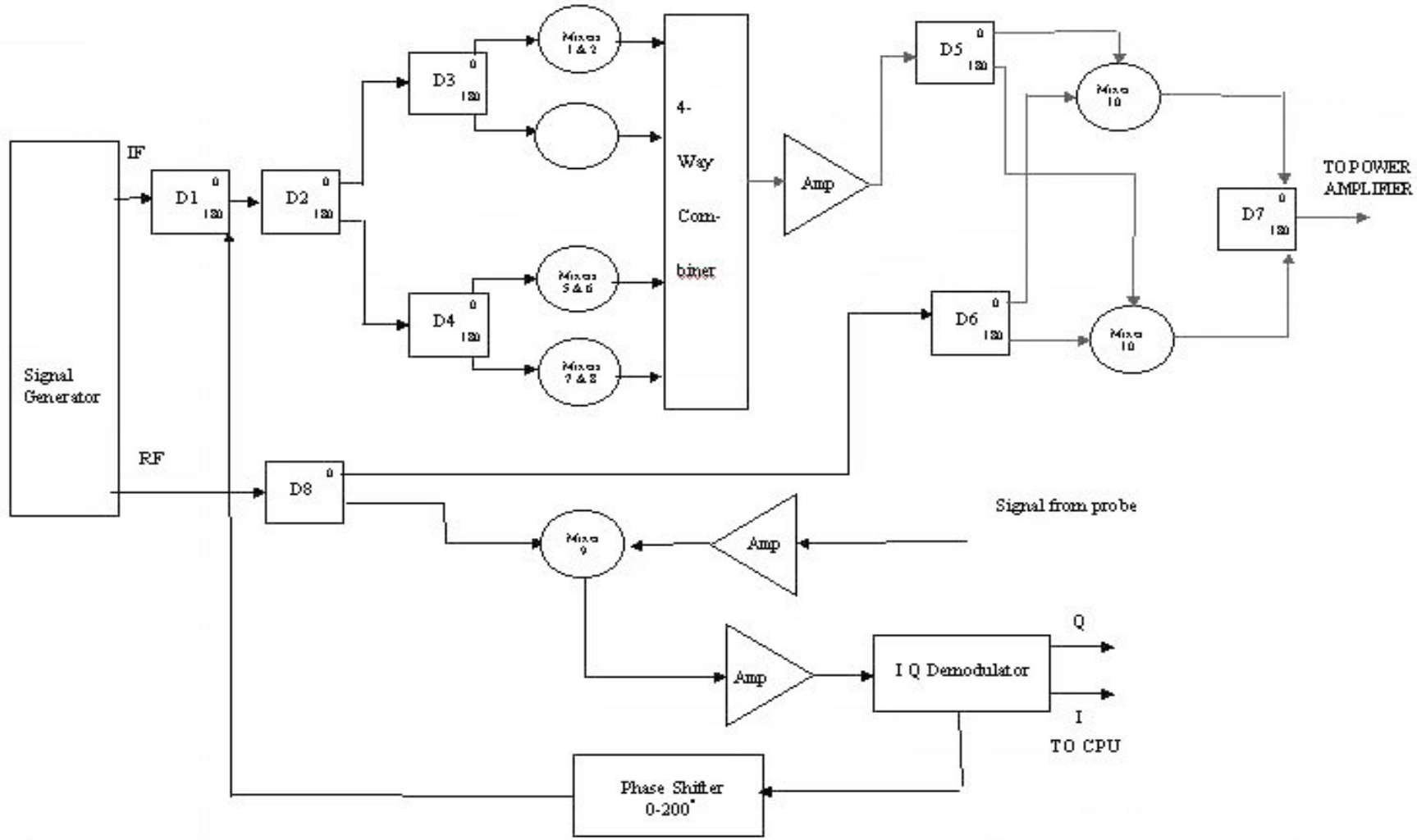
IF
RF
Signal Generator
D1
D2
D3
D4
D5
D6
D7
D8
0
120
Mixer 1 & 2
Mixer 5 & 6
Mixer 7 & 8
4-
Way
Com-
biner
Amp
Mixer 10
Mixer 10
TO POWER AMPLIFIER
Mixer 9
Amp
Signal from probe
Amp
I Q Demodulator
Q
I
TO CPU
Phase Shifter
0-200°

In the receiver stage the signal coming from the probe is first amplified and then mixed with the local oscillator signal in Mixer 9, which yields a signal at the IF terminal of 10MHz. It is again amplified and subsequently demodulated in the quadrature demodulator. The phase shifter provides a phase shift of 0-200° or an additional 180° phase shift if selected by the user. The real and imaginary outputs of the quadrature demodulator are passed to the computer and the signals are displayed in a graph in the program. The user can adjust the amplitude of the signal, introduce an offset of + / - 5V using the controls on the front panel.

The program that controls the spectrometer is written in LABVIEW and uses the data acquisition card DAQ PXI-6602 [33]. This is a timing and input/output card with eight 32bit counter/timers and 32 lines of TTL/CMOS compatible digital input/output. It generates a pulse sequence consisting of a trigger pulse and a series of two optional pulses. The user can specify the duration of the pulses (pulse width, in clock pulses of the computer), the delay before every pulse, the number of pulse sequences and their channel and the delay in between pulse sequences. The program also obtains the real and the imaginary part of the FID signal from the receiver using the NUDAQ PCI-9812 card [34], which is a 20Mhz, four-channel analog input card, and displays it on the screen as a graph. The delay times can be chosen to be linear, logarithmic, square rot or cube root. Finally the data is saved onto a file.

5.2 Signal Conduction Path

Consider figure 5.1. which shows a schematic diagram of the spectrometer and the coupling circuits. According to the values set by the user in the Labview program controlling the spectrometer, a pulse sequence is generated, using the data acquisition timer card (DAQ-6602), The pulse sequence is initiated by the trigger pulse, the first pulse in the sequence. The sequence is processed in the transmitter of the spectrometer as explained above and then fed to the 1-200MHz *amplifier*. The *attenuator* is switched manually to zero attenuation during pulse transmission and to high attenuation at other times so that delicate components do not get damaged by large sudden signals caused by voltage fluctuations or human error. From here the

signal is passed through the 20W, *power amplifier,* which has a frequency range from 10 to 250MHz, 20dB gain, and then to the *filter*. The circuit diagram of the filter is shown in figure 5.3. The coil of the filter, of inductance *L,* is tuned to the Larmor frequency. The crossed diodes block dc noise voltages whose amplitude is less than their transition voltage. As the diodes have a finite capacitance C_D they constitute together with the coil a LC filter which provides a high impedance at the Larmor frequency. The filtered signal is then fed to additional *crossed diodes*. These two elements isolate the power amplifier and its accompanying noise from the probe

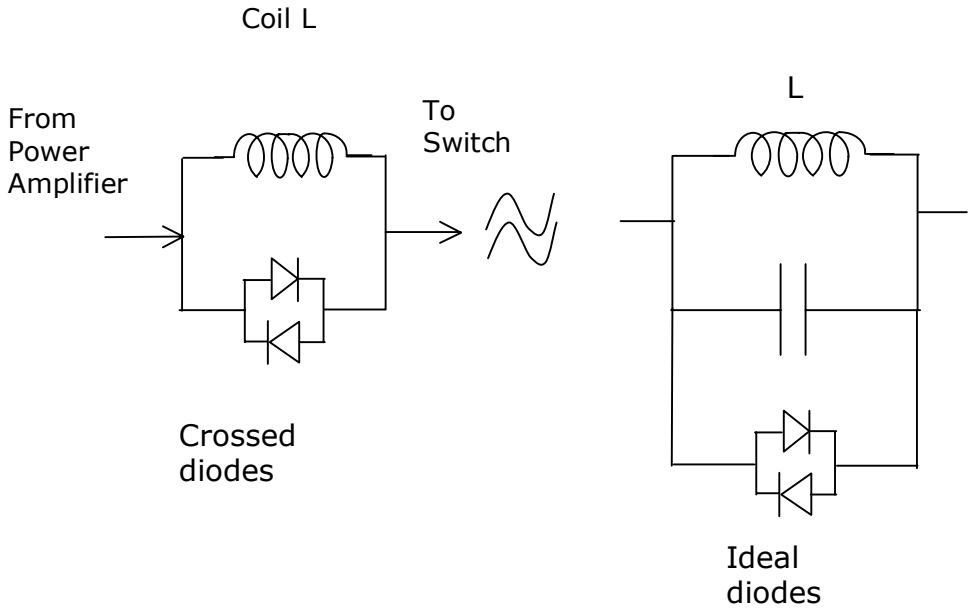

Figure 5.3: Diagram showing filter consisting of coil of inductance L, diode capacitance C_D and equivalent circuit.

circuit between pulses. The pulse then passes to the switch (figure 5.4), which passes the signal from the transmitter through the *splitter* (available from Minicircuits, Model Z-S-C-2-1) to the probe containing the sample or accepting the FID signal from the sample through the splitter and passes it on to the receiver. The switch is discussed in detail in the next section. The splitter has three terminals. The pulse from the transmitter is fed through one of these terminals and it is channelled by the splitter through another terminal, which also accepts the NMR signal from the probe and passes it back to the switch, which sends it on to the receiver through the crossed diodes and pre-amplifier. The crossed diodes are connected to the ground at the input

of the following preamplifier. The diodes cause a short connection at the pre-amplifier end when pulses are transmitted, which protects the delicate pre-amplifier from the large RF. power coming from the power amplifier. When the transmitter is switched off, the diodes are reverse biased due to the small voltage and thus act like an open circuit, which enables the NMR signal to pass through to the pre-amplifier. Another protection method is achieved when the quarter wavelength line in the switch is used. By virtue of having maximum impedance at λ/4, i.e. quarter wavelengths, the BNC cable acts like a transformer, which converts its output impedance according to the equation [35]:

$$Z_{input} = \frac{Z_0^2}{Z_{output}} \qquad (5.3)$$

where Z_0 =50Ω is the characteristic impedance of the transmission line. So, when a pulse is transmitted and the diodes cause a short connection to the pre-amplifier the receiving circuit is electrically disconnected from the probe owing to the infinite impedance of the transmission line (as Z_0=0).

From the pre-amplifier the NMR signal is fed into the receiver of the spectrometer which sends this data through the digitizing NUDAQ data acquisition card to the computer where it is processed by the Labview spectrometer control program to be displayed in graphical form.

5.3 The Switch

Figure 5.4 shows the switch, which either transmits the RF pulse from the transmitter to the coil to perturb the magnetization of the sample or accepts and passes to the receiver the NMR signal picked up by the coil from the sample. In the transmission mode, the high input voltage of the RF pulses of the order of 100V cause the diode arrangement D1 to conduct and forward the signal to the probe. During receiver mode D1 to the transmitter is reverse biased due to the weak strength of the single (≈ 1V) coming from the sample, and the signal solely passes to the receiver through the coil.

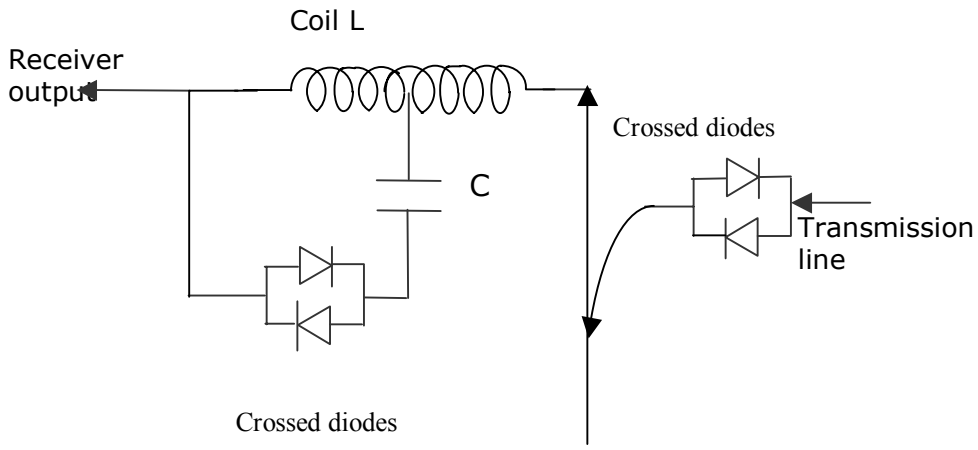

Figure 5.4: Coupling circuitry between transmitter, receiver and probe. For details see text.

The coil is designed using the following considerations. For example let the frequency

$$\nu = \frac{1}{2\pi\sqrt{LC}} \qquad (5.1)$$

be equal to 50MHz (calculated using $\nu = \gamma B / 2\pi$, where $\gamma = -7.45\times10^{7}$ rad $T^{-1}s^{-1}$ is the gyro magnetic ratio and B=4.2T is the field strength). L and C are the inductance of the coil and capacitance of the capacitor respectively. The circuit needs to be tuned to the impedance Z of the receiver, i.e. 50Ω. The impedance has to be purely resistive so its imaginary part has to be brought to zero, i.e. Z=R, where R is the resistance of the circuit: For the LC circuit used, we deduced the following relationship,

$$Z = \frac{L}{CR} = 50\Omega \qquad (5.2)$$

Using equations *(5.1)* and (*5.2)*, the value of L and C were calculated as L=159nH and C=63pF. Using a network analyzer to tune the circuit for 50Ω impedance and 50MHz frequency, the dimensions of the coil were estimated roughly utilizing $\nu \propto \frac{1}{\sqrt{LC}}$ and then found accurately using trial and error method. Thus, the

dimensions of the coil were obtained as length=70.10mm, number of turns=5 and diameter=14.67mm.

At a later time we realized that it would be advantageous if the inductance of the BN cable were used instead of the LC arrangement, which could cause saturation of the ferrite coil of the transformer used in the splitter. The modified switch circuit is shown in figure 5.5. In this scheme the quarter wavelength property of the BNC cable is utilized. At every quarter of the wavelength the impedance of the cable is maximum and the cable acts like an inductance coil. The wavelength of the material in vacuum λ_0, which gives maximum impedance, of the cable is calculated using $\lambda_0 = c/\upsilon$ as 1.71m. The wavelength in air, $\lambda = \lambda_0 / 1.5$, is 1.143m and $\lambda/4$ =29cm. The points of maximum impedance are at $\frac{\lambda}{4} + \frac{n\lambda}{2}$, where n=1,2,3, etc. Due to inherent inaccuracies of the network analyser, the same method, which was employed to find the dimensions of the coil, could not be used. A better procedure proved to be finding the length of the cable, which would give the same NMR signal as was found without the quarter wavelength cable. By this procedure the wavelength was found to be 8cm. The difference in the expected value (29cm) and the actual value for maximum impedance could be due the dielectric constant of the cable material.

5.4 Noise Considerations

The strength of the NMR signal is inherently very low as it is based on a very weak non-ionizing radio frequency phenomenon. Also the signal cannot be improved by varying the imaging parameters as it depends on the concentration of atoms in the sample. As amplification is the only method to increase the signal, the signal to noise ratio becomes very significant. The signal to noise ratio depends on the electronic equipment used in transmitting and receiving the signal and also the kind and number of nuclear spins. The frequency spectrum of noise varies according to the type of noise.

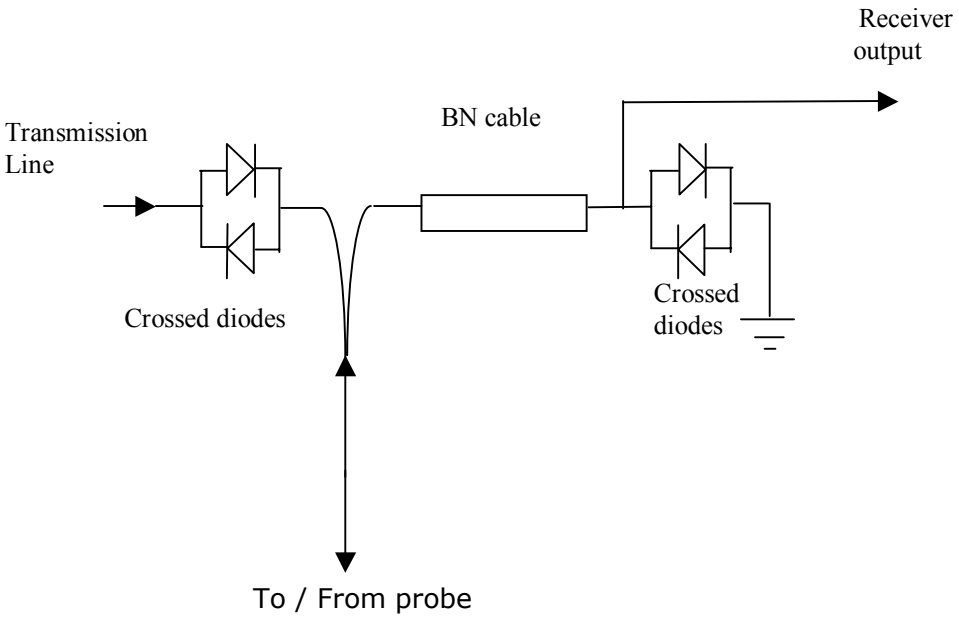

Figure 5.5: Diagram showing quarter wavelength line, which replaced coil and capacitor arrangement in switch.

Noise that is at a frequency different from the Larmor frequency is usually removed by filtering or using high gain-low noise amplifiers. Noise components at Larmor frequency can be reduced by signal averaging of a number of scan results [36] as the signal gets summed up faster than the noise. The signal increases as *n,* the number of accumulations, but the noise accumulation is proportional to only $\sqrt{n}$, the number of experiments, which in turn is directly proportional to the time *t* required to acquire the data. Thus the signal-to-noise ratio increases with $\sqrt{n}$. The disadvantage of this method is that it is not convenient when data have to be taken over a long period of time.

In our project, the main source of noise at frequencies other than the Larmor frequency in the transmission line was identified to be the power amplifier. A part of this noise was reduced by using the filter (figure 5.3), crossed diodes and quarter wavelength set-ups as explained in the previous section. Another complication arose, as the cooler of the power amplifier seemed to be generating a magnetic field, which created noise voltages in the transmission line. Separating the cooler and the power

amplifier physically reduced this noise by about a factor of three. The gain of the amplifier after the four-way combiner proved to be not sufficient enough. It was preset but could be increased internally. Further the transmitter on/off ratio was inadequate. The RF. gate, when switched on, ideally suppresses any pulses generated by the transmitter, but in practise a finite amount of current passes through it, even when the transmitter is switched off, which contributes to the noise. On the receiving side noise becomes a more serious problem due to the inherent weak strength of the NMR signal as discussed above. Unfortunately the amplitude of the noise we encountered at the output of the power amplifier was higher than the transition voltage of the crossed diodes and hence would be transmitted. We are now considering introducing an additional amplifier of 20dB gain in the receiver of the spectrometer between the mixer (M9) and the demodulator to strengthen the signal. Also, it is attempted to physically separate some of the receiver and transmitter signals so as to avoid interference between them.

CHAPTER 6
NMR RELAXATION IN SOLID XENON

6.1 INTRODUCTION

The aim of this project is the production of spin-polarised ^{129}Xe gas, using brute force method of ultra-low temperatures and high magnetic fields. To achieve this, NMR experiments were performed on the Xenon sample containing oxygen molecules as relaxant, to act as oxygen switch, and the polarisation and relaxation data obtained were analysed. The isotope of Xenon we used was naturally occurring ^{129}Xe, whose abundance in nature is 26.44%. The experimental details, procedure and the results are presented and discussed in this chapter. The NMR coil, creating the RF perturbation field, rotates the magnetization of the sample and also detects the FID signal as described in section 6.2. The temperature and field dependence of the polarisation and spin lattice relaxation time T_1 are shown in section 6.3 and the mechanism of the oxygen switch, its relative merits and demerits and the use of a nuclear relaxant, e.g. ^{3}He are discussed in section 6.4

Loading ^{129}Xe and oxygen into the sample cell

Xenon in gaseous form was loaded into the sample cell and the temperature was continuously lowered. At 165K, the boiling point of Xenon, it condensed and then became solid at 161K. At 100K, Oxygen gas was pumped into the sample cell, which was subsequently closed and the temperature of the system was further lowered. As Xenon in the solid form is very porous the O_2 molecules while gaseous or liquid can move in the free spaces in xenon ensuring mixing of xenon and oxygen when oxygen turns solid too at 54K.

6.2 THE NMR COIL

An external RF energy source, which is oscillating at the Larmor frequency of the nuclei of the sample, is required to perturb the magnetization vector. The RF energy is coupled to the sample cell by an RF NMR coil. We are using the same coil to transmit RF energy into the sample and to pick up the NMR signal generated by the sample. The sample probe holds the sample and the RF coil, (wound around the sample cell), which sends RF energy into the sample, and detects the signal emanating from the sample. The probe contains the coil, which is wound around the sample cell.

6.2.1 Coil Design Considerations [13] [14]

While choosing the coil design several factors have to be taken into consideration. RF coils store energy and resonate at the Larmor frequency of the sample nuclei. Their main constituents are an inductor of inductance L, or inductive elements, and a set of capacitive elements, of capacitance C. The inductor-capacitor circuit of the RF coil needs to be tuned to the sample frequency υ, given by:

$$\upsilon = \frac{1}{2\pi\sqrt{LC}}$$

An RF coil has a specific range of frequencies at which it resonates, proportional to the reciprocal of the quality factor Q. The range of resonant frequencies is affected by the conductivity of the coil and losses in the coupling to the coil. If the coil frequency is different from the resonant frequency of the sample nuclei, the coil will not efficiently generate the B_1 field nor efficiently detect the signal from the sample, as the net magnetisation is tipped through a smaller angle if the B_1 field is off resonance. This results in less transverse magnetization and less signal, leading to a poor signal-to-noise ratio. While designing the coil, several other factors have to be taken into consideration too. The coil should be able to generate intense fields without compromising sensitivity. To pick up the FID signal the B_1 field of the RF coil must be perpendicular to the direction of the static field. Also, the B_1 field should

be homogeneous over the sample volume. Otherwise, the spins will be tipped by different angles across the sample. Different RF coil designs devised to date include simple solenoid coils, which produce uniform fields but are unsuitable for high frequency applications due to their high inductance and stray capacitance. In addition, they are geometrically inconvenient to be placed in superconducting magnets. The Helmholtz coil consists of a large number of coil turns arranged on a sphere so that ideally a perfectly homogenous magnetic field is produced. When return paths for current are included, the Helmholtz coil is called a saddle coil. Another type of coil is the surface coil, which consists of simple wire loops that are tuned and matched to the required frequency. Their magnetic field decreases with distance and also they cannot penetrate very deeply. Most RF coils on NMR spectrometers are of the saddle coil design.

6.2.2 The Saddle Coil

The coil used in this project is basically of saddle design with the provision of having high or low resonant frequency, described by Zhang et al [37]. The circuit diagram is shown in figure 6.2.1, where L_s is the inductance of the sample coil, L_G and C_G are the elements that impedance match the circuit to 50 Ω and C_1, C_2, C_3 and L_1 are resonant frequency tuning elements. The coil can be set to transmit at high or low frequency by selecting input X or Y respectively. The equivalent circuit at high frequency is shown in figure 6.2.2. At high frequencies the impedance of C_2 is low, so it acts like a short to the ground, thereby isolating output X. The effective inductance of L_s and L_G is

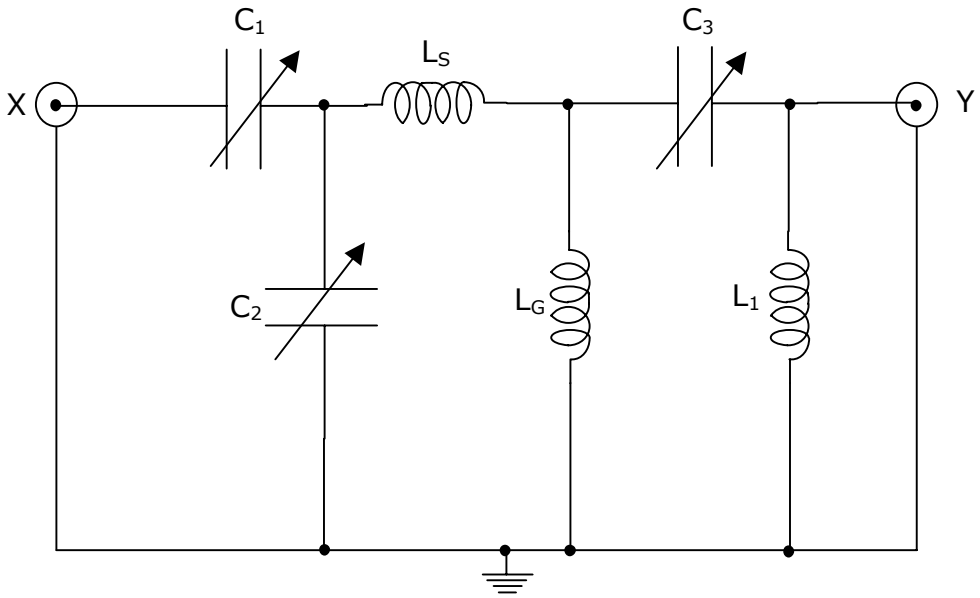

Figure 6.2.1: Electrical circuit of saddle coil, where L_S denotes the inductance of the coil containing the sample cell and L_G is the matching coil. C_1, C_2, and C_3 are variable capacitors used in impedance matching and to tune the coil.

$$L = \frac{L_S \cdot L_G}{L_S + L_G}$$

C_2 is used for tuning the coil to resonant frequency and L_4_is used to provide matching.

The equivalent circuit for low frequency is shown in figure 6.2.3. At low frequencies the impedance of capacitor C_3 is high and the effective inductance of L_s and L_G is:

$$L = L_s + L_G$$

Here C_1 and C_2 are used to tune the circuit to the resonant frequency ν and C_1 is used for impedance matching the circuit to 50 Ω.

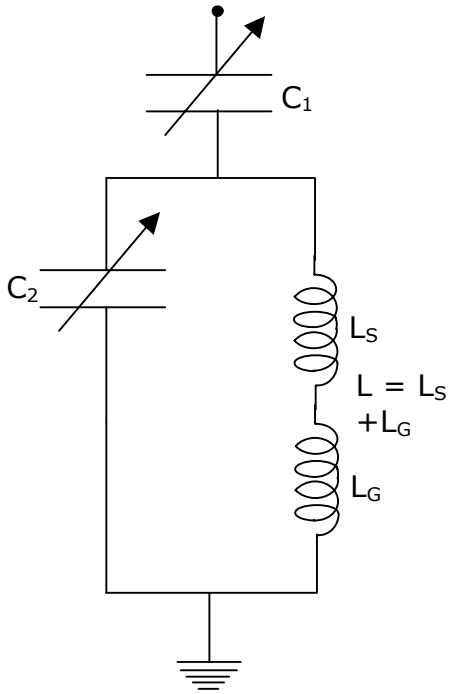

Figure 6.2.2: Equivalent circuit of coil at high frequencies. C_1 and C_2 are the tuning capacitors and C_1 is used for impedance matching. L_S and L_G are the sample coil and matching coil respectively

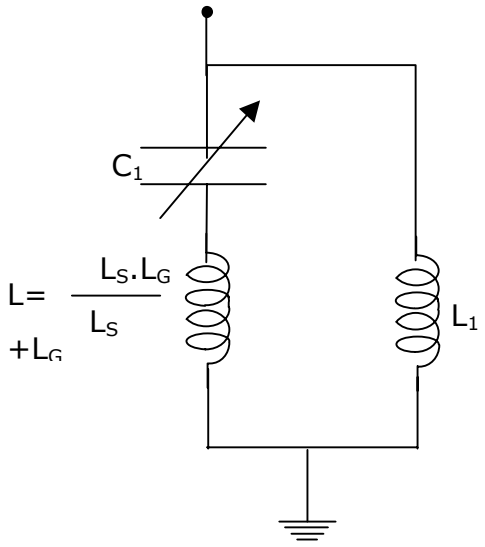

Figure 6.2.3: Equivalent circuit of coil at low frequencies. C_1 is the tuning capacitors. L denotes the total inductance of L_S and L_G.

Figure 6.2.4 shows the resonance of the coil at room temperature in a reflection measurement. It should be noted that the matching varies according to the temperature. Unfortunately it is difficult to measure the parameters and perform impedance matching once the coil is immersed in the mixing chamber.

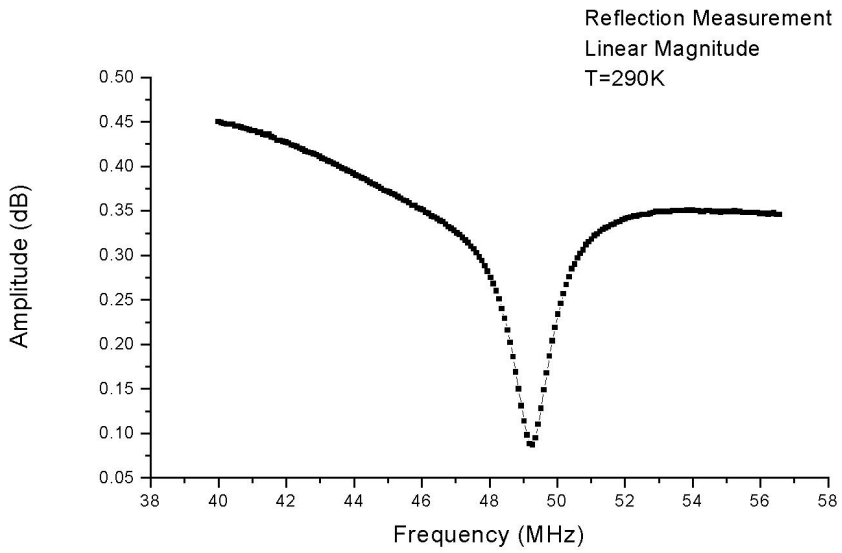

Figure 6.2.4: Graph showing resonance of coil at 49.62MHz during a reflection measurement performed at room temperature

6.2.3 The Probe

The probe holder is inserted directly into the mixing chamber inside the dilution refrigerator. It ends in the probe, which has numerous thin wires wound around it, which connect to the different thermometers and also the heater. The sample cell containing the xenon sample is located inside the NMR coil. A diagram of the saddle coil is shown in figure 6.2.4. The coil consists of Copper wires and the RF signal is transmitted to it by means of two 50Ω, stainless steel coaxial cables.

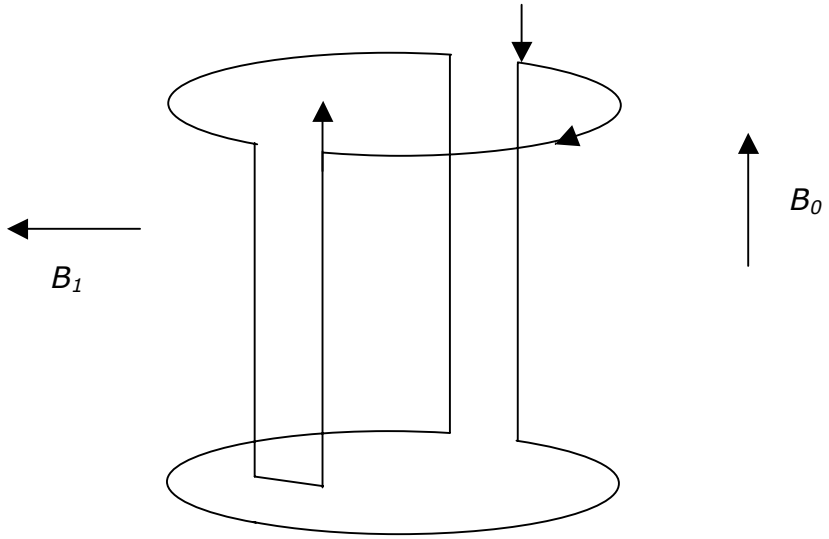

Figure 6.2.4: Saddle Coil showing signal input and output path. The current flows in clockwise direction as indicated. Directions of static field B_o and magnetic field applied through coil B_0 are as shown [38].

The coil consists of two turns, with current flowing in clockwise direction so the magnetic fields generated by each is in the same direction and the total field is equal to the sum of the individual fields. The coil is so placed so that the effective magnetic field B_1 is perpendicular to the static magnetic field B_0. The coil wound around the sample cell is placed in a metallic can, which provides electrical and magnetic shielding and is perforated at the bottom to ensure that the sample is immersed in the mixing chamber liquid. Figure 6.2.5 shows a photograph of the NMR coil surrounding the sample cell, above which the electrical coil circuit can be seen.

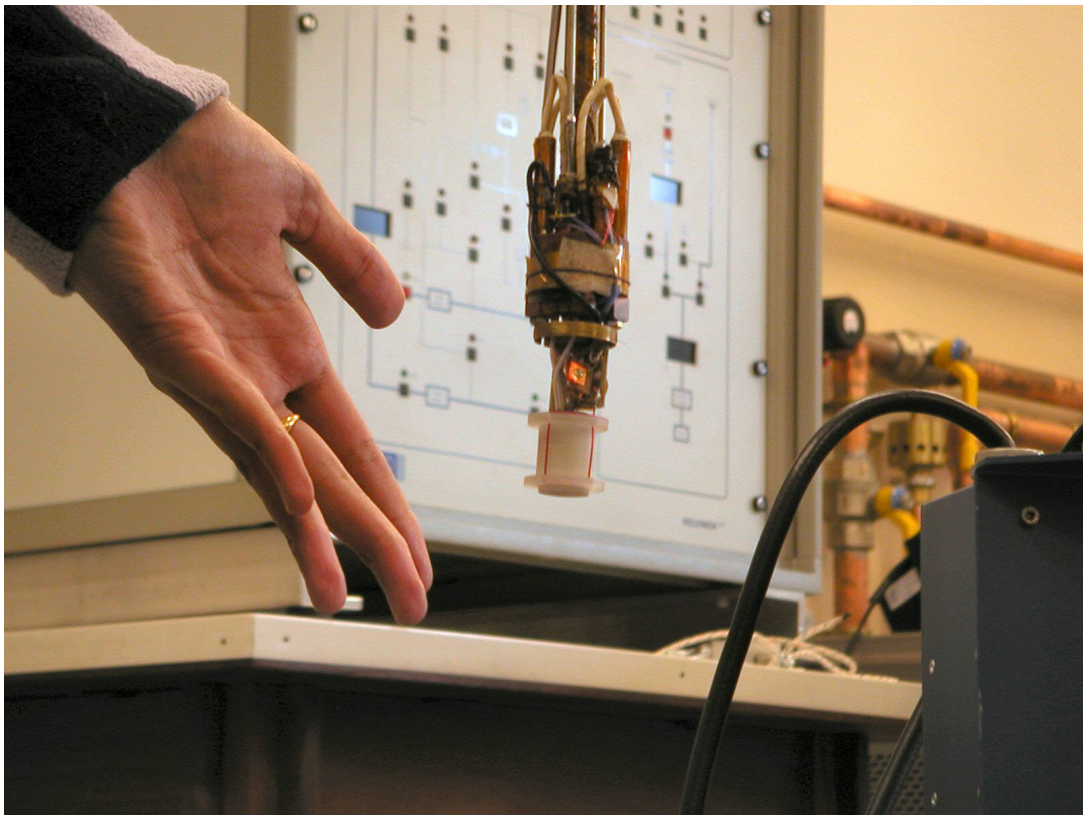

Figure 6.2.5: Photograph showing NMR coil wound around sample cell connected through electrical circuit to one end of the probe.

6.3 POLARISATION AND RELAXATION OF XENON

The sample cell containing the ^{129}Xe-O_2 mixture is inserted by means of the probe into the mixing chamber of the dilution refrigerator. NMR measurements are performed when the sample is in the field (15T) of the lower magnet. For relaxation studies, the sample can be lifted into the magnetic field (4.2T) of the upper magnet, where also the oxygen may be pumped out. The NMR signal was measured using the pulse sequence shown in figure 6.3.1. First a number of pulses, separated by very small delay times were transmitted to the sample to saturate the energy levels of the xenon nuclei. Then very small tipping pulses, after a time delay τ_2 after the saturation pulses were applied to measure the NMR signal. After each tipping pulse, an NMR signal is obtained. If $\tau_2 < \tau_1$, then the magnetization will not have recovered entirely and its magnitude will be less than at equilibrium.

The data we obtained when the delay time τ_2 was gradually increased is shown in figure 6.3.2. It can be seen that the amplitude increases with the delay time till it reaches the equilibrium value. The total time taken for the magnetization magnitude to completely recover to its equilibrium value gives T_1. The data obtained in this manner over a week is shown in figure 6.3.3. The magnetic field strength B was 14.86T, and hence the required Larmor frequency was calculated as $\upsilon = \frac{1}{2\pi}\gamma B$, where the gyromagnetic ratio for xenon γ =–7.45·10^7 rad T^{-1} s^1, resulting in a frequency of υ=175MHz.

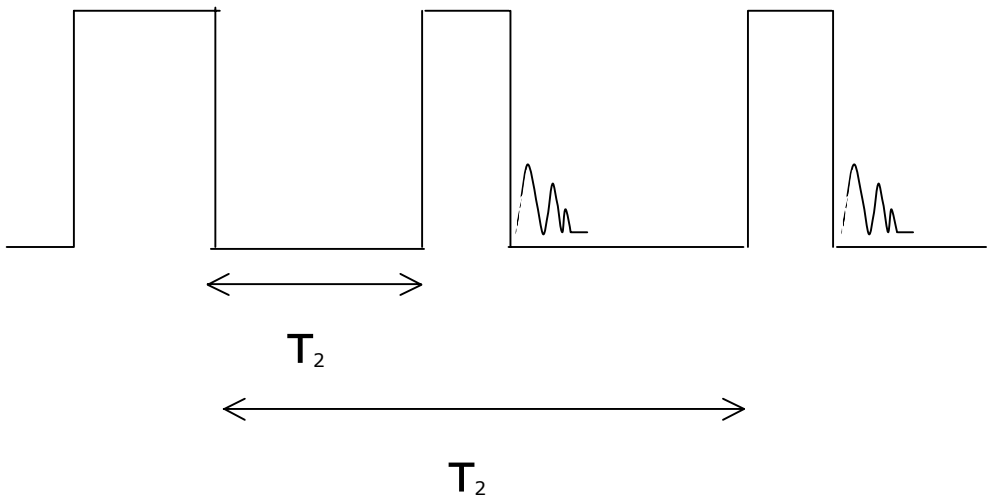

Figure 6.3.1 Pulse sequence showing one saturation pulse and smaller tipping pulses separated by saturation pulse by a time delay $\tau_{2,}$ followed by NMR signal (not drawn to scale).

It can be seen the magnitude of the signal amplitude increases and then reaches a constant value as the magnetization has fully recovered its equilibrium value. The spin lattice relaxation time T_1 is calculated using the following relation:

$$A(t) = A\left(1 - B\exp\left(\frac{-t}{T_1}\right)\right) \qquad (6.3.1)$$

Where $A(t)$=signal amplitude at time t, A=maximum amplitude and B=coefficient of saturation.

For the data obtained shown in figure 6.3.3, A=15822.8. Using B=1.011 and equation *(6.3.1)*, the spin-lattice relaxation time was calculated to be 727.775 minutes.

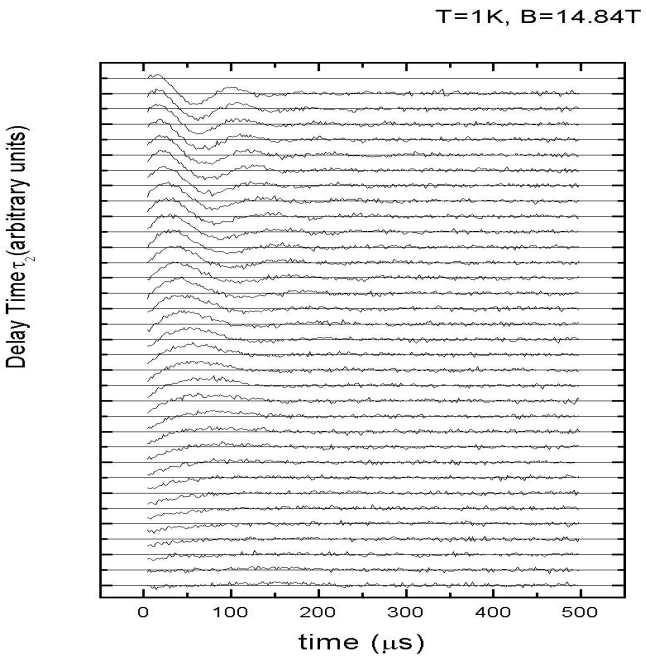

Figure 6.3.2: Graph showing the increase of signal amplitude as the delay time τ_2 is increased.

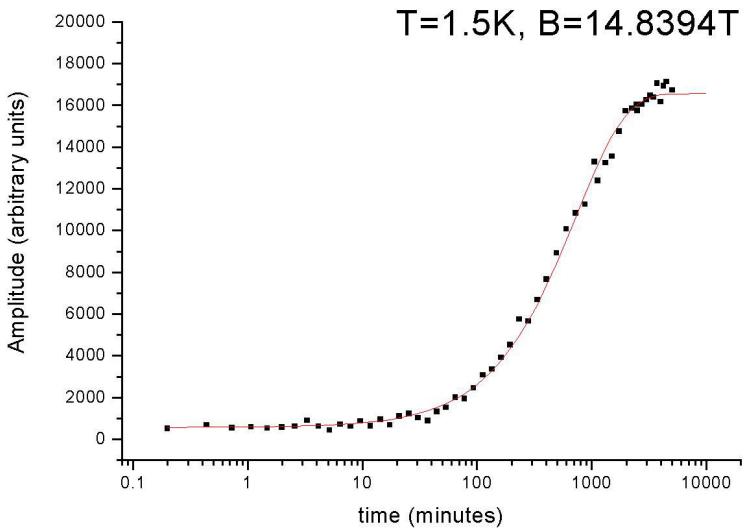

Figure 6.3.3: Graph showing increase of signal amplitude (FID) as a function of time. T_1=727.775 minutes.

6.3.1 Calculation of Field and Temperature Dependence of Polarisation

We derived an equation to calculate the theoretical polarisation of the Xenon sample given in equation *(6.3.9)* as given below with the following assumptions: The nuclear spins are independent of each other, the spin is uniformly ½, following Fermi-Dirac statistic (which determines the statistical distribution of fermions over the energy states for a system in thermal equilibrium). When the sample is subjected to a magnetic field the energy levels split into two, E_1 and E_2 of spin concentration N_1 and N_2 respectively with an energy difference of

$$E_1-E_2=\Delta E=h\upsilon, \qquad (6.3.2)$$

where h= 6.63 × 10^{-34} m^2 kg s^{-1} is Planck's constant. The difference in the spin concentrations is given by [13]:

$$\frac{N_2}{N_1}=\exp\left(\frac{-\Delta E}{k_B T}\right) \qquad (6.3.3)$$

Where k_B=1.38·$10^{-23}$$JK^{-1}$. If N_0 is the original spin concentration such that $N_0=N_1+N_2$, then using equation *(6.3.2), (6.3.3)* and $\upsilon=\gamma B$, we get,

$$N_1=N_0\exp\left(-\frac{\gamma B h}{2k_B T}\right) \qquad (6.3.4)$$

and

$$N_2=N_0\exp\left(+\frac{\gamma B h}{2k_B T}\right) \qquad (6.3.5)$$

The polarisation of the nuclear spin system is given by the ratio of the difference between the spin concentrations and the total spin concentration, i.e.:

$$P=\frac{N_2-N_1}{N_2+N_1}=\frac{N_0\exp\left(\frac{\gamma B h}{2k_B T}\right)-N_0\exp\left(\frac{-\gamma B h}{2k_B T}\right)}{N_0} \qquad (6.3.6)$$

Therefore,

$$P = \tanh \frac{\gamma Bh}{2k_B T} \qquad (6.3.7)$$

using $\mu=\gamma h$, we get

$$P = \tanh \frac{\mu B}{2k_B T} \qquad (6.3.8)$$

The decay of polarisation with time is taken into account with the factor $\left[1-\exp\left(\frac{-t}{T_1}\right)\right]$

Hence equation *(6.3.9)* becomes

$$P=\left[1-\exp\left(\frac{-t}{T_1}\right)\right]\tanh \frac{\mu B}{2k_B T} \qquad (6.3.9)$$

6.3.2 Temperature And Magnetic Field Dependence Of T_1

We measured the FID amplitude at different temperatures between 0.5K and 2K and plotted it against the corresponding relaxation time T_1 (figure 6.3.4). The T_1 decreases with increase in temperature as spin lattice relaxation occurs due to the energy transfer

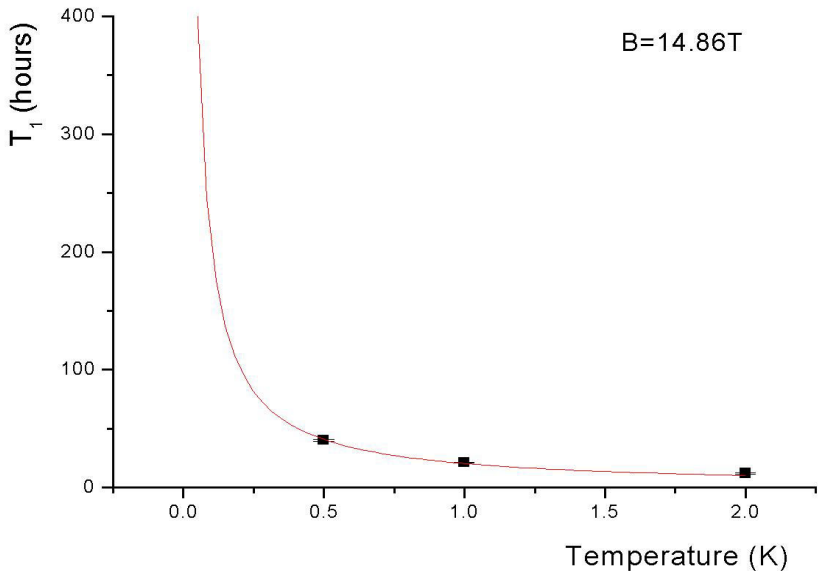

Figure 6.3.4: Graph showing spin-lattice relaxation T_1 as function of temperature T with B=14.86T. $T_1 \cdot \boldsymbol{T}$ =Constant=20.21

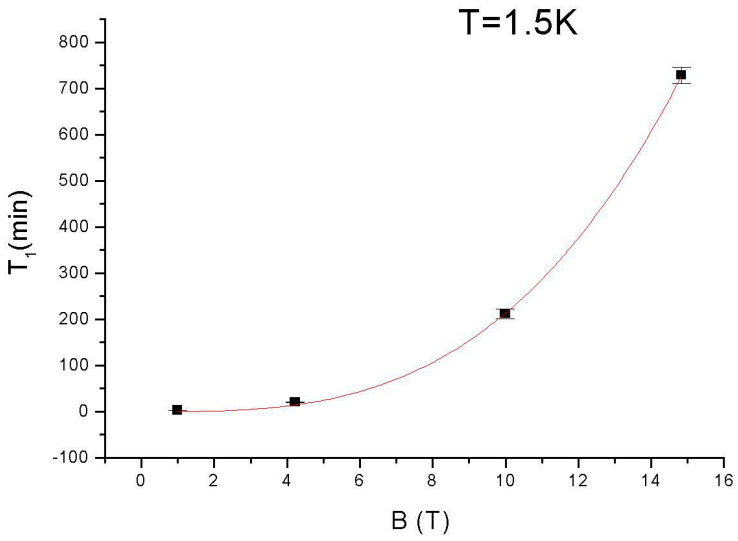

Figure 6.3.5: Graph showing magnetic field B dependence of T_1 at a temperature of 1.5K

of the nuclei to the surrounding lattice. The rate of energy transfer depends on molecular motion. As the translational of molecules increases with temperature, T_1 decreases. Also, it has been found from the data that the product of the spin lattice relaxation time T_1 and the temperature is constant and can be calculated from the slope of figure 6.3.4, i.e.

$T_1 \cdot \boldsymbol{T}$ =Constant=20.21

The dependence of the spin relaxation time T_1 on the magnetic field B is shown in figure 6.3.5. It can be seen that the spin lattice relaxation time increases with the strength of the magnetic field B.

From the experiments conducted and the data obtained it can be concluded that the spin lattice relaxation time T_1 exhibits stronger magnetic field dependence than temperature dependence, which may be aided by fluctuations in the magnetic fields generated by the oxygen electrons.

6.3.3 Temperature Dependence of Polarisation

Using equation *(6.3.9)*, we calculated the hypothetical polarisation for different temperature for a field strength B=14.86T over a time of t=48 hours (Figure 6.3.6 showing fractional polarisation as function of temperature). We have assumed that the product of T_1 and temperature T is a constant, i.e. $T_1T=20.21$ minK, calculated from figure 6.3.4. It can be seen that maximum polarisation should be achieved at a temperature about 0.035 K.

Figure 6.3.7 shows the polarisation as a function of B/T using equation *(6.3.9)*. It can be seen that the maximum polarisation obtainable for a field of 14.86T is 40% and occurs at about 30mK for a time period of 48h.

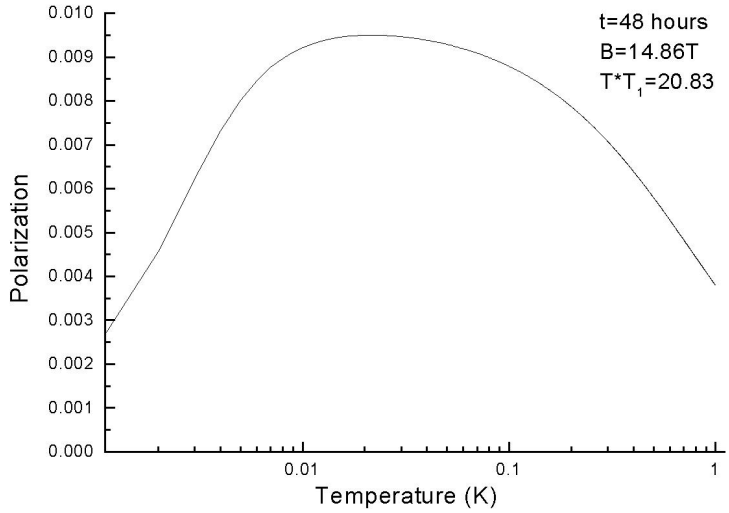

Figure 6.3.6: Graph showing theoretical polarisation as a function of temperature over 48 hours at a field strength of 14.86T using T_1T=20.21

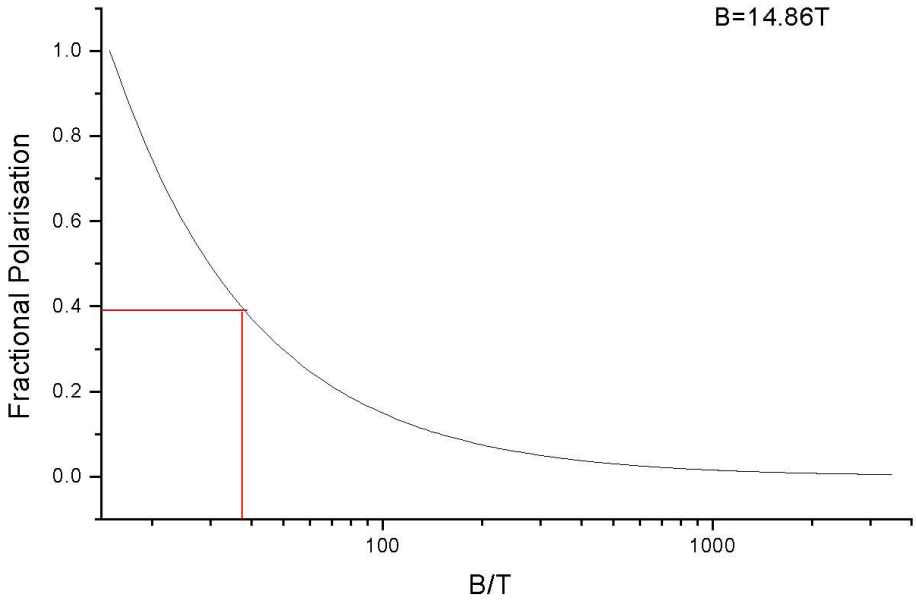

Figure 6.3.7: Graph showing theoretical polarisation as a function of field / temperature ratio *B/T* with magnetic field strength *B*=14.86T.

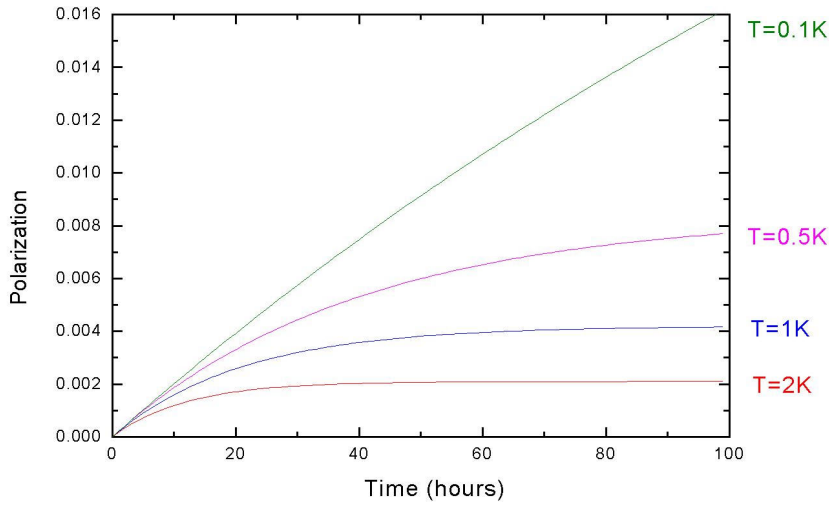

Figure 6.3.8: Graph showing growth of polarisation as function of time at temperatures of 0.1K, 0.5K, 1K and 2K in a field of strength 14.86T.

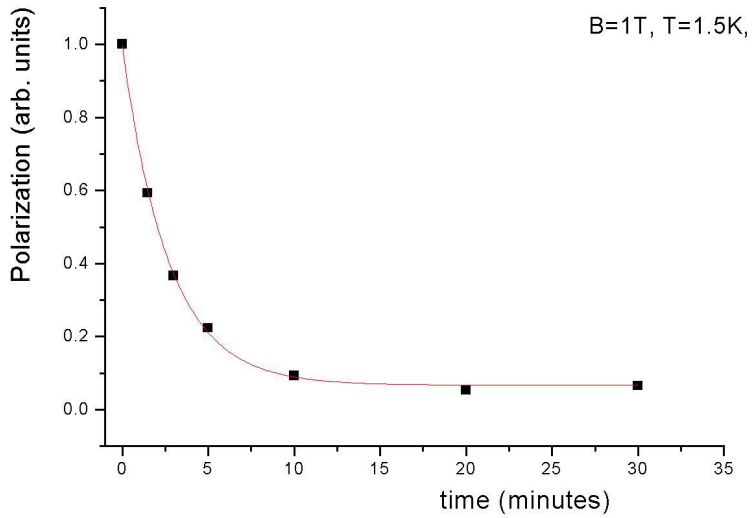

Figure 6.3.9: Graph showing measured polarisation decay as a function of time at 1.5K in a field of 1T.

The polarisation growth, obtained from FID data measured during rise of polarisation, at different temperatures as a function of time, is shown in figure 6.3.8, showing that at lower temperatures more polarisation is achieved

The decay of polarisation, obtained from the FID data we measured after the acquisition pulses were applied and relaxation was induced, is shown in figure 6.3.9, showing rapid demagnetisation.

6. 4 THE RELAXATION SWITCH

In the previous section, it was demonstrated that the spin-lattice relaxation time T_1 increases with an increase in B/T and that the maximum polarisation is achieved at ultra low temperatures and high magnetic fields. To achieve reasonable T_1 a relaxant has to be introduced into the sample, which accelerates the process of relaxation. Different types of relaxation switches have already been developed. Honig et al [9] have used ortho-H_2 impurities to achieve polarisation in HD. The ortho-H_2 spins are first coupled to the surrounding lattice of the material and then to HD through spin-spin interaction. Then HD is polarised with the relaxant removed by a process involving the change of ortho-H_2 to para-H_2 as Ortho-Hydrogen (in which the two protons of the diatomic hydrogen molecule have the same direction of spin) is at a higher energy state than the para form (having two protons with opposite directions of spin). They induce relaxation by retaining rotational angular momentum in their lowest state. Another method proposed by Honig uses radiation to introduce radicals into the HD sample, which increase the rate of relaxation at low temperatures. For ^{129}Xe, Honig proposes cooling of the cell, in which xenon is condensed by paramagnetic wires, which will induce relaxation, which is turned off by vaporising the sample, removing the wires and recondensing xenon. The method we used involves introducing paramagnetic oxygen into xenon, which induces electron relaxation. Honig successfully tested the removal of oxygen from xenon for a 0.2 cm^3 sample. We encountered several problems using the oxygen switch such as the freezing to immobility of the oxygen spins at ultra low temperatures or the impossibility of removing oxygen fast enough (at our working temperature of 100K) so as to not destroy the polarisation. The polarisation and relaxation results we obtained using the oxygen switch in the xenon sample are discussed in section 6.3. The problems of electron relaxation and the oxygen switch are analysed in the following sections and the use of ^{3}He as an alternative relaxant is discussed.

6.4.1 The Oxygen Switch

Relaxation due to paramagnetic oxygen arises by virtue of random fluctuations, in time, of the coupling energy between the spin magnetic dipole and the magnetic field in the lattice [36] [37]. The coupling of the xenon nuclei to the electron spin dipole of

oxygen provides the origin of relaxation. This dipole-dipole interaction depends on the nuclear spin, the electron spin, and the electron-nucleus distance. The magnetic field of the nuclear spin varies according $1/n^3$, and therefore proximity of the xenon nuclei to oxygen molecules is required. The electron spin depends on the amount and duration of the excitation energy applied and the spin lattice relaxation rate T_1 due to dipolar coupling with unpaired electrons is proportional to the average of the square of the interaction energy between electron spin of oxygen and the ^{129}Xe nuclei. Due to the large electron magnetic moment, at very low temperatures the electron spins are locked or frozen in, which inhibits the transition of the electron spins to a higher level. Thus, at low temperature, the resulting reduction of fluctuating magnetic field reduces the relaxation rate. In addition, the freezing of oxygen results in its immobility in xenon, leading to uneven distribution of oxygen electrons in the solid xenon.

Another problem encountered with the oxygen relaxation switch, is that if relaxation is achieved in very short times at a temperature of 100K, it is impossible to effectively pump out the oxygen before equilibrium is achieved, resulting in loss of polarization.

6.4.2 Future Work-The ^{3}He Relaxation Switch

Due to the problems enlisted, the use of a ^{3}He relaxation switch is considered. This relaxant works on the principle of nuclear relaxation, i.e. relaxation is induced by dipole-dipole coupling between nuclei, which results in fluctuations of the system's magnetic field. Candela [39] used the quantum tunneling of ^{3}He atoms near solid surfaces, which induces relaxation at arbitrarily low temperatures. ^{3}He does not freeze at the temperatures used in this project and it can therefore move inside the xenon sample and also, it can be evaporated at lower temperatures than oxygen which facilitates removal of the relaxation switch. Due to these advantages the utilization of ^{3}He as a relaxing agent has to be researched as the next step. However, for quantum tunneling of helium to occur a large surface area is necessary. We might have to use a substrate for xenon consisting of a porous substance with a large surface area, to ensure that maximum amount of ^{3}He is in contact with xenon. Biscup [40] for example used a silica gel substrate, with a specific high surface area, onto which xenon was plated.

CHAPTER 7
DISCUSSION

The following sections summarise the results and conclusion deduced on completion of this project. Certain areas that indicate scope for further work have also been highlighted.

7.1 CONCLUSION

The first two chapters of this report focused on the objective and the need for the project as well as providing the necessary background in NMR to the subject area under investigation. The subsequent chapters explained the preliminary work done which included mainly setting up the equipment to cool down the sample to temperatures below 10 K, i.e. the ^{3}He-^{4}He dilution refrigerator, the superconducting magnet system, which provides the static field B_0 and writing a program (in Labview), which generates the desired pulse sequence for the spectrometer. Noise in the NMR signal, whose main source was the power-amplifier in the transmitter path proved to be a significant obstacle, which could be partly overcome by modifying the power amplifier and partly by filtering. More work has to be done to bring noise to an absolute minimum in both the transmitter and the receiver path, so as to not mask the inherently small NMR signal.

An important by-product of temperature control was the investigation of thermometry for ultra-low temperatures and high magnetic fields. The working of the RuO_2 resistance thermometer, the tuning fork thermometer and the Coulomb Blockade thermometer was studied. Tuning fork thermometry, which is a novel concept devised by the research group of the University of Nottingham was found to be convenient to be used as a low temperature, field independent thermometer

especially owing to its easy set-up and inexpensiveness. It would be useful to probe deeper into the causes of the fluctuations of the quality factor and the resonance frequency with temperature when the tuning fork was immersed in helium, so as to be able to fit it to an empirical, reliable, working formula.

The main part of the work of the project was the NMR experiments performed on solid xenon containing oxygen with emphasis on determining the temperature and field dependence of the spin-lattice relaxation time T_1. The results are briefly summarized here again. The relationship between the polarization of the sample, the static magnetic field and the spin-lattice relaxation time can be described by

$$P=\left[1-\exp\left(\frac{-t}{T_1}\right)\right]\tanh\frac{\mu B}{2k_B T}$$

It was determined theoretically that for a polarisation time of two days the optimum polarization achievable in a field of 14.86T is about 40% and occurs approximately at 30mK. From the experimental data it could be seen that the amount of polarisation that can be achieved increases with decrease in temperature. An interesting result was the finding that the product of temperature and T_1 is constant, enabling us to calculate the theoretical T_1 or polarization for fixed field strength. It was found out that the curve of the T_1 plotted against the magnetic field strength B at fixed temperature is best described by $T_1=AB^n$ and the best fit is obtained when n=3. As predicted, the T_1 increases with decrease in temperature, especially below 0.5K and decreases with increase in field. It was realized that the electron relaxation by oxygen was not efficient enough due to the following problems: The electron spins freeze at very low temperatures disabling the relaxation mechanism. We assume that the fluctuations in the magnetic fields generated by the electron spins hamper the relaxation mechanism too. Another problem encountered was the problem in pumping out oxygen from the sample. This process has to take place at around 100K at which the T_1 is short and therefore might result in loss of polarisation, as it is difficult to pump out the oxygen fast enough.

7.2 FUTURE WORK

The use of ^{3}He in the xenon sample, inducing relaxation by nuclear dipole-dipole interaction, is suggested as a possible relaxant. The ^{3}He is expected not to freeze at the working temperatures and also removal of ^{3}He will be easier as ^{3}He can be evaporated at temperatures much lower than the boiling temperature of oxygen. However, it may be necessary to use a porous substance with a large surface area to act as a substrate for the xenon solid also allowing ^{3}He to be mobile. (It is the mobility and motion of the ^{3}He that will induce relaxation in the ^{129}Xe.) After the ^{3}He relaxation switch has been developed, experiments will have to be performed to test field and temperature dependence of T_1.

The equipment needs certain improvement. In particular, the noise of the spectrometer has to be lowered further. Different amplifier models will have to be tried out to find the highest gain and signal-to-noise ratio. It is hoped to increase the amplification by about 20 times. The fact that at times the transmitter sends out RF signals even in between pulse generation has to be investigated. This poses serious problems as undesired RF signals might destroy the polarisation or heat the sample. The saddle coil used to induce magnetization in the sample and detect the FID signal is not very flexible owing to its two outputs of low and high frequency. The construction of a coil having a single resonant frequency has to be considered. Also the sensitivity and the impedance matching of the coil have to be improved.

CHAPTER 8

BIBLIOGRAPHY

[1] Navon G., Song Q., Rõõm T., Appelt S., R. E. Taylor R., Pines A, *Science* **271**, 1848, (1996)

[2] Leduc M., Nacher P., Sinatra A., Tastevin G., Choukeife J., Bittoun J., Darrasse L., Guillot G., Maitre X., Durand E., Vignaud A., *Hyperpolarized ^{3}He Gas M.R.I,* Laboratoire Kastler Brossel and Unité de Recherche en Résonance Magnétique Médicale, http://www.lkb.ens.fr/recherche/flquant/HPG.html, (June 2003)

[3] Bifone A., Song Y., Seydoux R., Taylor R., Goodson B., Pietrass T., Budinger T., Navon G., Pines A., *Proc. Natl. Acad. Sci. USA,* **93**, 12932, (1996)

[4] Mugler J., Bogorad P., Driehuys B., Brookeman J., Nuclear Magnetic Resonance Using Hyperpolarised Noble Gases, to be published in *Journal of Magnetic ResonanceAnalysis,*
http://imaging.med.virginia.edu/hyperpolarized/ref/review.pdf, (August 2002)

[5] Rubin S., Spence M., Pines A., Wemmer D., *J. Magn Reson.,* **152**, 79, (2001)

[6] www.webelements.com (July 2003)

[7] Albert M., Cates G., Driehuys B., Happer W., Saam B., Springer C., Wishnia A., *Nature,* **370,** 199 (1994)

[8] Wong G., Tseng C., Pomeroy V., Mair R., Hinton D., Hoffmann D., Stoner R., Hersman F., Cory D., Walsworth R., *J. Magn Reson,* **141**, 217, (1999)

[9] Honig A., Wei X., Lewis A., Haar E., Seraji-Bozorgzad K., *Physica B,* **284-288**, 2049, (2000)

[10] Bloch F., *Physical Review,* **70**, 460 (1946)

[11] Goldman M., *Quantum Description of High-Resolution NMR in Liquids*, Clarendon Press, Oxford Science Publications (1995)

[12] Khandpur R., *Handbook of Biomedical Instrumentation,* Tata McGraw-Hill Publishing Company Ltd., (2001)

[13] Shung K., Smith M., Tsui B., *Principles of Medical Imaging,* Academic Press Inc., (1992)

[14] Hornak J., The Basics of MRI, copyright 1996-2003, http://www.cis.rit.edu/htbooks/mri/

[15] Pobell F., Matter and Methods at Low Temperatures (2^{nd} edition*)*, Springer (1996)

[16] Oxford Instruments, Tubney Woods, Abingdon, Oxon, OX13 5QX, United Kingdom

[17] J.H. Naish, Ph.D. Thesis, University of Nottingham (1997)

[18] Muirhead C., Temperature Measurement and Control, Low Temperature Techniques Course, Institute of Physics (2002)

[19] Greywall D., *Phys. Rev. Lett.*, **B33**, 7520 (1986)

[20] Bradley I., Cryogenic Techniques below 1K, Low Temperature Techniques Course, Institute of Physics (2002)

[21] Nanoway, CBT Primary Thermometer Instruction Manual, Nanoway Oy, Ylistönmäentie 26,FIN-40500 Jyväskylä, Finland

[22] Clubb D., Ph.D. Thesis, University of Nottingham (2003), http://etheses.nottingham.ac.uk/archive/00000007/01/Thesis02.pdf (June 2003)

[23] Rychen J., Ihn T., Hermann A., Ensslin K., Hug H., van Schendel J., Guentherodt H., *Phys. Rev. Lett.*,**71**, 1695 (2000)

[24] Grober R., Acimovic J., Schuck J., Hessman D., Kindlemann P., Hespanha J., Morse A., Karrai K., Tiemann I., Manus S., *Rev. Sci. Instr.*, **71**, 2776. (2000)

[25] Kittel C., Kroemer H., Thermal Physics (2nd Edition), W.H. Freeman and Company (1980)

[26] Schroeder D., An Introduction to Thermal Physics, Addison Wesley Longman Publications (2000)

[27] Zeegers J., de Waele A., Gijsman H., *J. Low. Temp. Phys.*, **84**, 37 (1991)

[28] Bharthwaj A., Angappane S., Srinivasan D., Natarajan T., Rangarajan G. and Wessling B., Proc. International Cryogenic Engg., Conference 18 (2000)

[29] L. Michalski, K. Eckersdorf, J. Kucharsky, Temperature Measurement (2nd Ed.), Wiley Publications (1991)

[30] Pekola J., Hirvi K, Kauppinen J. and Paalanen M., *Phys. Rev. Lett.*, **73**, (1994)

[31] D.K. Ferry, (1995), Quantum Mechanics, (Institute of Physics: Bristol)

[32] Farhangfar Sh., Hirvi K., Kauppinen J., Pekola J., Toppari J., Averin D. and Korotkov A., *J. Low Temp. Phys.,* **108**, 191 (1997)

[33] National Instruments Corporation, NI PXI-6602, 11500 N Mopac, Expwy, Austin, Texas 78759-3504

[34] Adlink Technology Inc., NUDAQ PCI-9812, 9F, No. 166, Jian Yi Road, Chungho City, Taipei, Taiwan, R.O.C.

[35] J. Kirsch, R. Newman, A Pulse NMR experiment for an undergraduate physics laboratory, Massachusetts Institute of Technology, http://web.mit.edu/8.13/www/JLExperiments/JLExp_12AJP.pdf

[36] E. Fukushima, S.Roeder, Experimental Pulse NMR, Addison-Wesley Publishing Company, (1981)

[37] Zhang Q, Zhang H., Lakshmi K., Lee D., Bradley C., Wittebort R., *Journal of Magnetic Resonance,* **132,** 167, (1998)

[38] Belohrad D., Kasal M., Institute of Scientific Instruments, Academy of Sciences of the Czech Republic, Kralovopolska 147, CZ - 612 64 Brno, Czech Republic, http://www.isibrno.cz/~belohrad/radioelektronika2000-saddlecoilformri.pdf

[39] Candela D., Kalechofsky N., Low Temperature Hyperpolarisation Of Xenon ½, Oxford Instruments America Inc, http://www.oxford-instruments.com/SCNRMP15.htm

[40] Biscup N., Low Temperature Hyperpolarisation of Xenon, *Research Matters,* **15**, 4 (2002)